

Modeling heat dominated electrical breakdown

PROEFSCHRIFT

ter verkrijging van de graad van doctor aan de
Technische Universiteit Eindhoven, op gezag van de
rector magnificus, prof.dr.ir F.P.T. Baaijens, voor een
commissie aangewezen door het College voor
Promoties in het openbaar te verdedigen
op maandag 25 juni 2018 om 13.30 uur

door

Ashutosh Agnihotri

geboren te Kanpur, India

Dit proefschrift is goedgekeurd door de promotoren en de samenstelling van de promotiecommissie is als volgt:

voorzitter: prof.dr.ir. G.M.W. Kroesen
1^e promotor: prof.dr. U.M. Ebert
2^e promotor: prof.dr. W.H. Hundsdorfer† (Radboud University, Nijmegen)
copromotor: dr. E. Camporeale (CWI)
leden: prof.dr.ir. B. Koren
 prof.dr. N.J. Lopes Cardozo
 prof.dr. V.L. Guerra (Instituto Superior Tecnico, Lisbon)
lid: prof.dr. D.T. Crommelin (Universiteit van Amsterdam)

Het onderzoek of ontwerp dat in dit proefschrift wordt beschreven is uitgevoerd in overeenstemming met de TU/e Gedragscode Wetenschapsbeoefening.

This work is part of the Industrial Partnership Programme (IPP) Computational Sciences for Energy Research (project number: 12CSER058) of the Foundation for Fundamental Research on Matter (FOM), which is part of the Netherlands Organisation for Scientific Research (NWO). The CSER initiative is co-financed by Shell Global Solutions International B.V. The research was conducted at Centrum Wiskunde & Informatica (CWI). CWI is the national research institute for mathematics and computer science in the Netherlands. CWI is part of the Institutes Organisation of NWO.



A catalogue record is available from the Eindhoven University of Technology Library

ISBN: 978-90-386-4543-8

Copyright © 2018 by A. Agnihotri.

All rights are reserved. No part of this publication may be reproduced, stored in a retrieval system, or transmitted, in any form or by any means, electronic, mechanical, photocopying, recording or otherwise, without prior permission of the author.

Contents

1	Introduction	1
1.1	Electrical breakdown	1
1.2	Lightning and other types of electrical discharges	2
1.3	Research objectives addressed in the thesis	3
1.4	Structure of the thesis	4
2	Physical models and numerical test cases	7
2.1	Physical models	8
2.1.1	Drift-diffusion-reaction equations	8
2.1.2	Electric field	9
2.1.3	Euler equations	9
2.2	Numerical method	10
2.2.1	Spatial discretization	10
2.2.2	Temporal discretization	12
2.3	Some numerical test cases	14
2.3.1	2D Streamer simulation	14
2.3.2	1D Euler simulation	15
2.3.3	2D Euler simulation	16
3	Coupling discharge and gas dynamics in streamer-less spark formation in supercritical N₂	19
3.1	Introduction	20
3.2	Description of the model	21
3.2.1	Model for the electric discharge	21
3.2.2	Model for the background gas	22
3.2.3	Coupling between discharge and gas dynamics	22
3.3	Simulation conditions	23
3.3.1	Boundary conditions	23
3.3.2	Initial conditions	24
3.3.3	Numerical method	24
3.4	Results and discussion	24
3.5	Summary and outlook	26

4	Modeling heat dominated electric breakdown in air, with adaptivity to electron or ion time scales	29
4.1	Introduction	30
4.2	Model formulation	31
4.2.1	Model for the electric discharge dynamics	31
4.2.2	Boundary conditions for the discharge	32
4.2.3	Model for the gas dynamics	33
4.2.4	Boundary conditions for the fluid equations	34
4.3	The reduced model on the ion time scale and time adaptivity to electron or ion dynamics	35
4.3.1	Motivation and problem statement	35
4.3.2	Derivation of the reduced model on the ion time scale	35
4.3.3	Numerical test of the reduced model on the ion time scale	37
4.3.4	Computational adaptivity to electron or ion time scale	41
4.4	Simulation and results	42
4.4.1	Set-up of the model	42
4.4.2	Simulation results	43
4.5	Summary and Outlook	49
4.6	Numerical Implementation	49
4.6.1	Computation of electron density in reduced model	50
4.6.2	Implementation of heating term in Euler system	52
4.6.3	Implementation of outflow boundary condition in the Euler system	52
5	Adaptive selection of sampling points for uncertainty quantification	53
5.1	Introduction	54
5.2	Mathematical methods	57
5.2.1	Clenshaw-Curtis (CC) quadrature rule	57
5.2.2	Selection of collocation points based on hierarchical surplus	58
5.2.3	Multiquadric biharmonic radial basis	59
5.2.4	New adaptive selection of collocation points	60
5.3	Numerical examples	61
5.3.1	Case 1: $g(x) = \arctan(10^3 x^3)$	63
5.3.2	Case 2: $g(x) = \frac{1}{(2+\sin(3\pi x))^2}$	65
5.3.3	Case 3: Lotka-Volterra model (predator-prey)	66
5.3.4	Case 4: Van der Pol oscillator	69
5.4	Conclusions and future work	72
6	Conclusions & Outlook	75
6.1	Conclusions	76
6.2	Outlook	77

Acknowledgements	89
Curriculum Vitae	91
Summary	93
Scientific Contributions	95

Chapter 1

Introduction

1.1 Electrical breakdown

An electrical breakdown process is said to occur when a current flows through an otherwise non-conducting medium (insulator) when subjected to a sufficiently high voltage. This flow of current may be a transient flow or a continuous one (such as an electrical arc). The ability of a medium to resist a current flow when subjected to increasing voltages is characterized by its *dielectric strength*. For instance, the dielectric strength of air at atmospheric pressure is 3×10^6 V/m. In the picture below, one can observe filamentary structure around the Tesla coil. The high electric field around the coil causes the air to ionize allowing current to leak into the air in colorful filamentary features.



Figure 1.1: Tesla coil demonstrating electrical breakdown process.

1.2 Lightning and other types of electrical discharges

To study the phenomenon of electrical breakdown is complex due to its multiscale character. Natural atmospheric lightning provides the most popular form in which the phenomenon may be observed. Lightning is a *very* large scale electric discharge process where the cloud(s) and the ground together act as electrodes and the atmospheric air in between as the insulating medium. Lightning stays a subject of modern research [1, 2].

Apart from atmospheric lightning, electrical breakdown has been studied as a fundamental physical process and due to its many applications. Depending on the application and the experimental conditions, different types of electrical discharges may be produced. A classification may be made based on characteristics such type of voltage applied (pulsed, AC or DC voltage), whether the discharge is stationary or transient, non-linear effects such as space charge, based on the role of heating and complexity of the chemistry involved. Some forms include:

- **Streamer discharge**

It is a finger shaped, cold transient discharge characterized by a thin layer of space charge around its head. It is capable of penetrating non-ionized media due to the strong electric field enhancement at the tips. Streamers are efficient at activating chemical pathways. As a result they have found applications in cleaning polluted media [3, 4, 5] and sterilizing wounds [6, 7]. They have also been employed for airflow control around the wings of an aircraft in the aerospace industry [8, 9].

- **Dielectric barrier discharge (DBD)**

It is an electric discharge that occurs between two electrodes which have layers of insulating dielectric material (dielectric barrier) between them. Frequently, the voltage source to operate DBD uses an alternating current (AC). In industry they were first used in the process of ozone production [10]. Other applications include polymer surface treatment, semiconductor manufacturing, plasma display panels etc [11]. They have also been successfully employed in the field of plasma medicine [12] and for treatment of textiles [13].

- **Spark and arc discharge**

It is characterized by gas heating. When a strong electric current flows through a medium, the electrical energy is converted to heat energy causing the gas temperature to rise. The increased temperature results in increased pressure which leads to gas expansion. Due to this the density of the gas drops locally. This results in a reduction in the *reduced* electric field (E/N where N is the neutral gas number density) which makes it favourable for

the current to keep flowing along the heated path thereby further promoting the electrical breakdown of the gas.

A spark/arc discharge can be detrimental to high-voltage equipment or it can be the mode of operation. For example, in high power switching, effort is being put to understand the properties of super-critical fluids [14] or high pressure CO₂ [15, 16] so as to use them as an eco-friendly power switching medium in electrical circuit breakers.

Spark discharges are also used for ignition purposes in internal combustion engines [9]. In the field of wireless communication, a spark-gap transmitter is used which uses an electric spark to create radio frequency radiation [17].

In the current thesis, our goal is to understand the role of heating in an electrical breakdown phenomenon, and to develop efficient computational models to simulate it.

A key motivation for studying electrical breakdown phenomena comes from high voltage technology. In particular, the transition to renewable energy sources such as sun and wind requires efficient transmission of electrical energy. For instance, energy harvested at a remote off-shore wind farm has to be transmitted with minimal losses to areas of high consumption. This can be achieved by transmitting electricity at lower frequencies than 50 Hz or even by setting up direct current (DC) transmission lines over long distances. To effectively balance supply and demand, a grid should be established. For control of current flow in the grid, electrical switches/circuit breakers are used. Sulphur-hexa fluoride SF₆ has been the dominant switching medium used in these breakers/switches due to its excellent interruption properties such as high dielectric strength and short dielectric recovery time. However, SF₆ is an extremely strong greenhouse gas with toxic by-products. This creates a need for investigating new media that are environment friendly and have excellent switching properties. Consequently, experimental testing and simulations should be performed to study electrical breakdown in these new media.

1.3 Research objectives addressed in the thesis

The current thesis deals with the *development* and *application* of efficient computational models to simulate heat driven electrical breakdown in various media. Coupling the electric discharge model to the gas dynamics model is essential to building a successful model which can then be employed to simulate the process. Such a coupling poses various challenges. These are briefly described below:

- The dynamics of an electric discharge is highly non-linear due to the coupling of the electric field and the charge densities and the transport coefficients (function of reduced electric field). Furthermore, the discharge

model should be able to resolve the relevant length scales, such as thin space charge layers (if they occur) of few microns in atmospheric air and the electrode gap, which differ by orders of magnitude.

- The gas dynamics model must be able to resolve spatial features such as shocks waves (pressure, density) which determine the reduced electric field and hence the transport coefficients.
- A major computational challenge arises when combining the widely varying time scales between the model describing the electrical discharge dynamics and the gas dynamics. On the one hand we have the electrons moving on the nanosecond timescale. On the other hand we have the ions which move relatively slower on the microsecond timescale. Lastly, we have the neutral gas as well which moves on even longer timescales (the timescale of movement of the gas depends on the gas temperature). Certainly, resolving the fastest timescale provides the most accurate description but is computationally too demanding for long timescales. This motivates the need for different models resolving the different time scales, and for a hybrid approach to switch between these models.

This thesis focuses on the objectives mentioned above and makes an effort to develop a computational model that may be utilized for simulating electrical discharge phenomena where heating plays a significant role. On a holistic level, the model developed may possibly be integrated in the suite of tools available for electric discharge simulation.

1.4 Structure of the thesis

Apart from the current chapter, this thesis has been divided into 5 Chapters. Below is a short outline of the contents of each of the chapters.

- **Chapter 2**

This chapter focuses on the physical models employed for discharge modelling and presents a few numerical test cases. These test cases are essential for the accuracy of numerical results presented later.

- **Chapter 3**

This chapter has been adapted from the article *Coupling of discharge and gas dynamics in streamer-less spark formation in supercritical Nitrogen* published in the Japanese Journal of Applied Physics.

- **Chapter 4**

This chapter has been adapted from the article with the title *Modelling heat dominated electric breakdown in air, with adaptivity to electron or ion time scales* published in the journal Plasma Sources Science and Technology.

- **Chapter 5**

This chapter discusses a new strategy for selecting sampling points for uncertainty quantification. It has been adapted from the article published with the above-mentioned title in the International Journal for Uncertainty Quantification.

- **Chapter 6**

This chapter summarizes the results presented in the thesis and ends with an outlook on the future challenges.

Chapter 2

Physical models and numerical test cases

In this chapter we present an overview of the physical models employed in this thesis. We also review the numerical discretization techniques used for our simulations and present some numerical test results.

2.1 Physical models

In the current work, we focused on modeling the dynamics resulting from coupling of electric discharge and the surrounding gaseous medium. We chose a fluid modeling approach to model the electric discharge as well as the surrounding gas.

2.1.1 Drift-diffusion-reaction equations

In fluid modeling of an electric discharge we consider charge densities $n(\mathbf{r}, t)$; in contrast to Particle-in-cell models that model individual particles in the system. The time evolution of the charge density of a particular species i is given by an equation of the form

$$\frac{\partial n_i}{\partial t} + \nabla \cdot \mathbf{j}_i = S_i. \quad (2.1)$$

In the above equation, n_i , \mathbf{j}_i and S_i are functions of position and time. n_i and \mathbf{j}_i are density and current density of species i and S_i represents the sum total of all the sources and sinks for species i .

The expressions for the terms \mathbf{j}_i and S_i depend on the complexity of the model and on the physical processes included in the model. For our current purposes, we consider the *first-* order model for electric discharge where \mathbf{j}_i is given by

$$\mathbf{j}_i = \mu_i n_i \mathbf{E} - D_i \nabla n_i + \mathbf{v} n_i, \quad (2.2)$$

where μ_i denotes the mobility and D_i denotes the diffusion coefficient of the species i respectively. The first term in the above expression is the advective (*drift*) part and the second term is the diffusive part. Also, \mathbf{v} denotes the velocity of the background medium. For a more accurate description, higher order fluid models can be derived as velocity moments of Boltzmann equation [18, 19]. The first-order model suffices for the work presented in this thesis.

The term S_i contains the information about the reactions between different charged/neutral species in the system. For instance, for the impact ionization represented by reaction



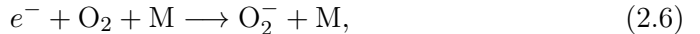
the source term is modeled by

$$S_{imp} = k(E/N)n_e[\text{N}_2], \quad (2.4)$$

where k is the reaction coefficient whose value depends on the *reduced* electric field E/N where N is the gas number density and n_e and $[\text{N}_2]$ represent the electron and nitrogen density, respectively.

An important *sink* process to consider in electric discharge simulations in air is the process of attachment represented by the reactions





where the former reaction is a two-body attachment process and the latter is a three-body attachment process and M is another molecule.

Photo-ionization is yet another important *non-local* source of electrons. Due to its non-local character, it cannot be modeled by reactions such as for impact ionization and attachment processes. For the purpose of the work presented in this thesis, we do not include photo-ionization in the source terms. A detailed discussion about the role of photo-ionization in electric discharge simulations (in particular streamer discharges) and its implementation can be found in the PhD theses of Anna Dubinova [20] and Jannis Teunissen [21].

Depending on the questions to be addressed, the reaction set representing the source and the sink can be made as complete as needed comprising numerous neutral and charged species. This provides accurate description of the physics but poses a computational challenge which at times may be prohibitive. As a result, a careful choice has to be made about which species to include in the model.

2.1.2 Electric field

The evolution of the electric discharge occurs under the influence of the electric field which is a combination of the external electric field and the electric field generated by the electric discharge itself. We compute this electric field self-consistently with the Poisson equation

$$-\nabla^2 \phi(\mathbf{r}, t) = \frac{q(\mathbf{r}, t)}{\epsilon_0}, \quad (2.7)$$

where ϕ is the electric potential, q is the charge density and ϵ_0 is the permittivity of free space. The electric field \mathbf{E} is computed from the electric potential via the relation

$$\mathbf{E}(\mathbf{r}, t) = -\nabla \phi(\mathbf{r}, t). \quad (2.8)$$

In this thesis, we chose a direct solver that uses LU factorization to solve the resulting linear system.

2.1.3 Euler equations

To model the gas dynamics, we adopt the compressible Euler equations without viscosity. The relevant equations for the conservation of mass, momentum and

energy are in cylindrical coordinates

$$\frac{\partial \rho}{\partial t} + \nabla \cdot (\rho \mathbf{v}) = 0, \quad (2.9)$$

$$\frac{\partial (\rho v_r)}{\partial t} + \nabla \cdot (\rho v_r \mathbf{v}) = -\frac{\partial p}{\partial r}, \quad (2.10)$$

$$\frac{\partial (\rho v_z)}{\partial t} + \nabla \cdot (\rho v_z \mathbf{v}) = -\frac{\partial p}{\partial z}, \quad (2.11)$$

$$\frac{\partial \xi}{\partial t} + \nabla \cdot (\mathbf{v}(\xi + p)) = S_\xi, \quad (2.12)$$

with $\mathbf{v} = (v_r, v_z)$ and $\nabla = (\partial_r, \partial_z)$. Here ρ is the gas mass density, \mathbf{v} the gas velocity, p is gas pressure, and

$$\xi = \rho \epsilon + \frac{1}{2} \rho v^2 \quad (2.13)$$

is the total energy per unit volume. ϵ is the internal energy per unit mass; it is related to pressure through the ideal gas law

$$p = \rho \epsilon (\Gamma - 1), \quad (2.14)$$

where Γ is the heat capacity ratio for the background gas whose value we assume to be constant and equal to 1.4 for air. Furthermore, S_ξ is the energy source term that models gas heating. More details about the form of S_ξ are discussed later in Chapter 4 of this thesis.

2.2 Numerical method

In this section we describe the numerical methods employed to computationally solve the physical model described above. We adopt a method-of-lines approach where we first carry out spatial discretization of a PDE (or a system PDEs) which then results in an ODE (or a system of ODEs). This ODE (or a system of ODEs) is then numerically integrated in time.

2.2.1 Spatial discretization

For the spatial discretization of time-dependent advection-diffusion-reaction equations and the Euler equations we adopt a finite volume method on a uniform grid. In a finite volume method, we use the integral form of the equations (conservation laws/continuity equations) and hence instead of talking of point values we talk about cell-averaged quantities. Also, the conservative form is well suited to problems where shocks/discontinuities are expected.

To explain the spatial discretization clearly, consider the general form of a conservation law which is given by

$$\frac{\partial n}{\partial t} + \nabla \cdot \mathbf{F} = S, \quad (2.15)$$

where n is the physical quantity to be solved for, \mathbf{F} denotes the *flux* function and S denotes the source term. As explained before, in a finite volume method the computational domain is divided into *cells*. For the computations carried out in this thesis, we chose a uniform cylindrical domain with azimuthal symmetry. This resulted effectively in a uniform Cartesian grid with the r and z directions as the two axes. A grid cell can be annotated by

$$C_{i,j} = [(i-1)\Delta r, i\Delta r] \times [(j-1)\Delta z, j\Delta z] \quad (2.16)$$

where i and j are positive integers indexing the r and z directions respectively and Δr and Δz are the cell width (spatial resolution) in either direction. Integrating the equation 2.15 over a cell $C_{i,j}$ we get

$$\frac{dn_{i,j}}{dt} = \frac{1}{r_i\Delta r} \left(r_{i-\frac{1}{2}} F_{i-\frac{1}{2},j} - r_{i+\frac{1}{2}} F_{i+\frac{1}{2},j} \right) + \frac{1}{\Delta z} \left(F_{i,j-\frac{1}{2}} - F_{i,j+\frac{1}{2}} \right) + S_{i,j} \quad (2.17)$$

For the sake of completeness (as our electric discharge model contains an advective component and a diffusive component in the flux function), we further breakdown the flux function \mathbf{F} into an advective component \mathbf{F}^a and a diffusive component \mathbf{F}^d . For the advective component we use an upwind scheme [22] with flux limiting which is defined as

$$F_{i+\frac{1}{2},j}^a = E_{r;i+\frac{1}{2}}^+ (n_{i,j} + \psi(P_{i,j})(n_{i+1,j} - n_{i,j})) \quad (2.18)$$

$$+ E_{r;i+\frac{1}{2}}^- \left(n_{i+1,j} + \psi \left(\frac{1}{P_{i+1,j}} \right) (n_{i,j} - n_{i+1,j}) \right), \quad (2.19)$$

$$F_{i,j+\frac{1}{2}}^a = E_{z;j+\frac{1}{2}}^+ (n_{i,j} + \psi(Q_{i,j})(n_{i,j+1} - n_{i,j})) \quad (2.20)$$

$$+ E_{z;j+\frac{1}{2}}^- \left(n_{i,j+1} + \psi \left(\frac{1}{Q_{i,j+1}} \right) (n_{i,j} - n_{i,j+1}) \right), \quad (2.21)$$

where $E^+ = \max(\mu E, 0)$ and $E^- = \min(\mu E, 0)$ differentiate the upwind directions for the two components E_r and E_z of the electric field. Note that for positive charge carriers μ carries a positive sign and a negative sign for the negative charge carriers. Furthermore, we have

$$P_{i,j} = \frac{n_{i,j} - n_{i-1,j}}{n_{i+1,j} - n_{i,j}}, \quad (2.22)$$

$$Q_{i,j} = \frac{n_{i,j} - n_{i,j-1}}{n_{i,j+1} - n_{i,j}}. \quad (2.23)$$

The function ψ is the Koren limiter function [23] whose form is given by the expression

$$\psi(\theta) = \max \left(0, \min \left(1, \frac{1}{3} + \frac{\theta}{6}, \theta \right) \right). \quad (2.24)$$

The diffusive component of the flux function \mathbf{F}^d is computed using a second-order central difference scheme as below

$$F_{i+\frac{1}{2};j}^d = \frac{D}{\Delta r} (n_{i,j} - n_{i+1,j}), \quad (2.25)$$

$$F_{i,j+\frac{1}{2}}^d = \frac{D}{\Delta z} (n_{i,j} - n_{i,j+1}). \quad (2.26)$$

Discretization of the Poisson's equation

The electric potential is computed in the cell centers by using a second-order central difference of the Poisson's equation

$$\frac{\phi_{i+1,j} - 2\phi_{i,j} + \phi_{i-1,j}}{\Delta r^2} + \frac{\phi_{i+1,j} - \phi_{i-1,j}}{2r_{i,j}\Delta r} + \frac{\phi_{i,j+1} - 2\phi_{i,j} + \phi_{i,j-1}}{\Delta z^2} = -\frac{q_{i,j}}{\epsilon_0} \quad (2.27)$$

In this thesis, we chose a direct solver that uses LU factorization to solve the resulting linear system.

The components of the electric field \mathbf{E} are computed at the cell *faces* by using the relation $\mathbf{E} = -\nabla\phi$ as below

$$E_{r;i+\frac{1}{2},j} = -\frac{\phi_{i+1,j} - \phi_{i,j}}{\Delta r}, \quad (2.28)$$

$$E_{z;i,j+\frac{1}{2}} = -\frac{\phi_{i,j+1} - \phi_{i,j}}{\Delta z}. \quad (2.29)$$

The modulus of the electric field is needed to compute the reduced electric field E/N which is further used to calculate the mobility and diffusion coefficients. The modulus of the electric field is computed at the cell centers as below

$$E_{i,j} = \sqrt{\left(\frac{E_{r;i-\frac{1}{2},j} + E_{r;i+\frac{1}{2},j}}{2}\right)^2 + \left(\frac{E_{z;i,j-\frac{1}{2}} + E_{z;i,j+\frac{1}{2}}}{2}\right)^2} \quad (2.30)$$

2.2.2 Temporal discretization

After we have carried out the spatial discretization, we end up with a system of ODEs which then can be numerically integrated in time. For our purpose, we employed the explicit trapezoidal rule, a second order Runge-Kutta method, for time discretization with time step Δt . Given a time instant $t_k = k\Delta t$ and values of physical quantities \mathbf{n}_k at that time instant, the values at the next time instant t_{k+1} are computed by first computing an intermediate result using a Forward Euler method

$$\tilde{\mathbf{n}}_{k+1} = \mathbf{n}_k + \Delta t F(\mathbf{n}_k), \quad (2.31)$$

and thereafter computing the final values as

$$\mathbf{n}_{k+1} = \mathbf{n}_k + \frac{\Delta t}{2} F(\mathbf{n}_k) + \frac{\Delta t}{2} F(\tilde{\mathbf{n}}_{k+1}) \quad (2.32)$$

Explicit time-stepping methods, such as the one above, are simple to implement but have to follow a time step restriction determined by the Courant-Friederichs-Levy (CFL) condition for stability. There are other restrictions from the diffusion and reaction components of the equations (the system describing the electric discharge) [22] but they are dominated by the CFL criterion for the advective component. We chose a value of 0.25 for the Courant number in our case which is well below the maximum required for stability of the method.

We have applied the same numerical discretization procedure to Euler equations as well.

2.3 Some numerical test cases

We present snapshots of test cases of the simulation with the code that was developed to carry out the modeling work presented later on in this thesis.

2.3.1 2D Streamer simulation

The 2D streamer simulation result presented below was performed with the parameters described in [24]. The result accurately captures the space charge and electric field strength.

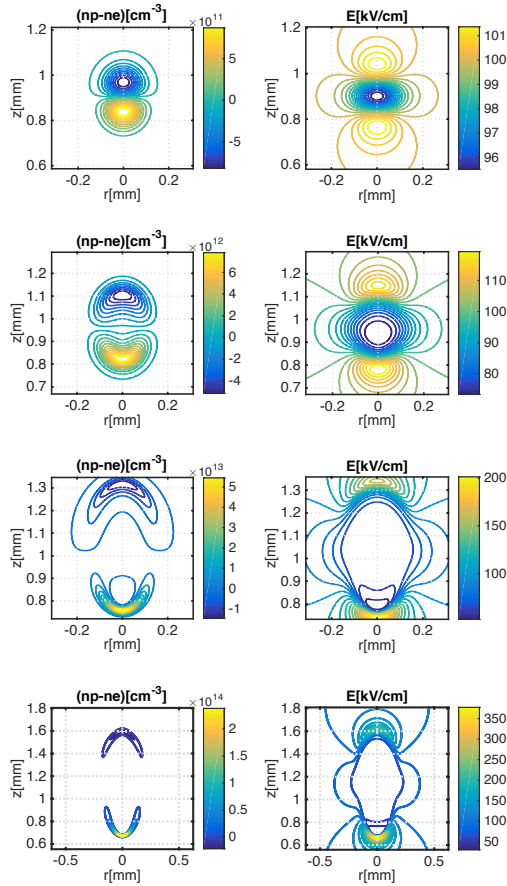


Figure 2.1: Streamer Simulation: The numerical solution of the drift-diffusion-reaction model for pure N_2 in a uniform background field. The background field point in the negative z -direction and has a strength of 100 kV/cm . Initially, a neutral Gaussian seed with peak density of $4.8 \times 10^{10} \text{ cm}^{-3}$ was placed at $z = 0.833$ mm . Shown are the space charge and electric field strength at times $t = 0.225$ ns , 0.375 ns , 0.525 ns and 0.675 ns (time increases from top to bottom).

2.3.2 1D Euler simulation

To test the solver for the Euler equations in 1D we used the Sod shock tube test [25]. It is commonly used to test the accuracy of CFD codes. The following initial conditions were used,

- pressure left = 1.0, pressure right = 0.1,
- density left = 1.0, density right = 0.125,
- velocity left = 0.0, velocity right = 0.0,
- length = 1.0,
- duration = 0.125.

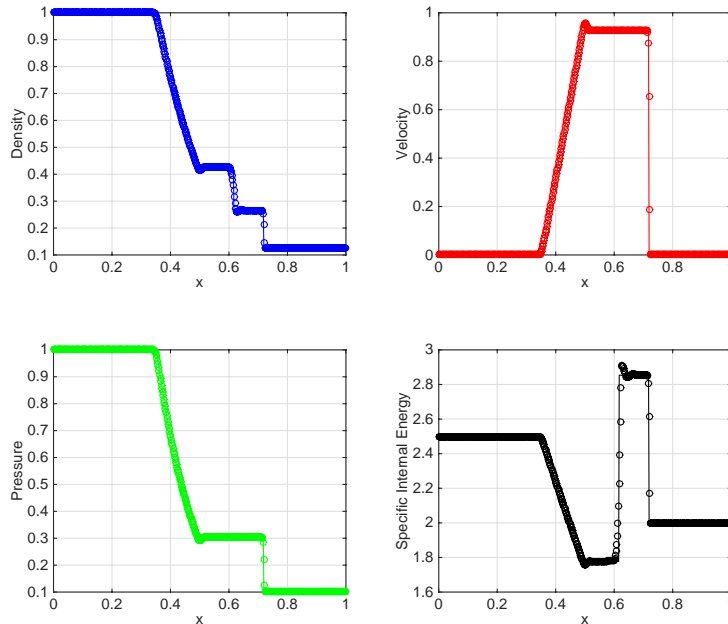


Figure 2.2: 1D Euler Simulation: Plotted are the physical quantities versus the position for the 1D Sod tube test at time $t = 0.125$ s. The analytical solution is plotted with continuous line and the computed solution is plotted with circles. The simulations were performed on a 1D grid of 600 cells with a CFL number of 0.25.

2.3.3 2D Euler simulation

To test the gas dynamics solver in 2D, we used the 2D Riemann problems described in [26] as test cases. To set the initial data for the 2D Riemann problem, the computational domain was partitioned into four quadrants

$$(p, \rho, v_x, v_y)(x, y, 0) = (p_1, \rho_1, v_{x_1}, v_{y_1}), \text{ if } x > 0.5 \text{ and } y > 0.5, \quad (2.33)$$

$$= (p_2, \rho_2, v_{x_2}, v_{y_2}) \text{ if } x < 0.5 \text{ and } y > 0.5, \quad (2.34)$$

$$= (p_3, \rho_3, v_{x_3}, v_{y_3}) \text{ if } x < 0.5 \text{ and } y < 0.5, \quad (2.35)$$

$$= (p_4, \rho_4, v_{x_4}, v_{y_4}) \text{ if } x > 0.5 \text{ and } y < 0.5. \quad (2.36)$$

Below we plot results for two initial conditions. The figures in the left column are from the reference article [26] and the figures in the right column are computed from our code.

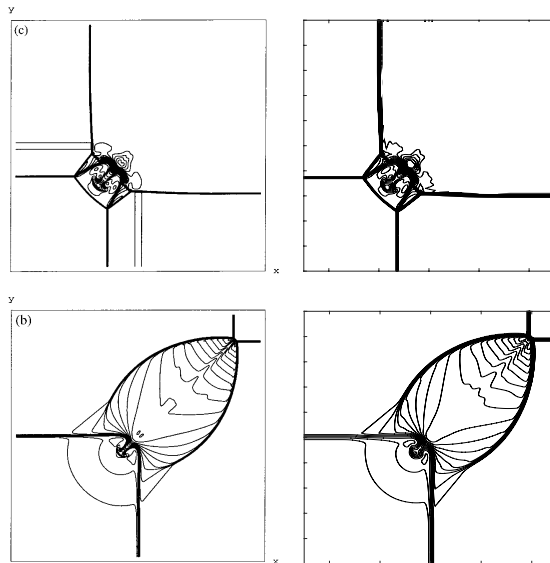


Figure 2.3: 2D Euler Simulation: Shown are the density contour plots at time $t = 0.25$ (first row) and $t = 0.3$ (second row) for a set of two initial conditions. The simulations were performed on a 600×600 grid with a CFL number of 0.25.

For the figure in the first row the initial condition is

$$p_2 = 0.300 \quad \rho_2 = 0.5323 \quad p_1 = 1.500 \quad \rho_1 = 1.500$$

$$v_{x_2} = 1.206 \quad v_{y_2} = 0.000 \quad v_{x_1} = 0.000 \quad v_{y_1} = 0.000$$

$$p_3 = 0.029 \quad \rho_3 = 0.138 \quad p_4 = 0.300 \quad \rho_4 = 0.5323$$

$$v_{x_3} = 1.206 \quad v_{y_3} = 1.206 \quad v_{x_4} = 0.000 \quad v_{y_4} = 1.206$$

For the figure in the second row the initial condition is

$$\begin{aligned} p_2 &= 1.000 & \rho_2 &= 1.000 & p_1 &= 0.400 & \rho_1 &= 0.5313 \\ v_{x_2} &= 0.7276 & v_{y_2} &= 0.000 & v_{x_1} &= 0.000 & v_{y_1} &= 0.000 \\ p_3 &= 1.000 & \rho_3 &= 0.800 & p_4 &= 1.000 & \rho_4 &= 1.000 \\ v_{x_3} &= 0.000 & v_{y_3} &= 0.000 & v_{x_4} &= 0.000 & v_{y_4} &= 0.7276. \end{aligned}$$

Chapter 3

Coupling discharge and gas dynamics in streamer-less spark formation in supercritical N₂

A two-dimensional cylindrically symmetric model is developed to study the streamer-less spark formation in a short gap on the timescale of ion motion. It incorporates the coupling between the electric discharge and the gas through the heat generated by the discharge and the consecutive gas expansion. The model is employed to study electrical breakdown in supercritical N₂. We present the simulation results of gas heating by the electrical discharge and the effect of gas expansion on the electrical discharge.

1

¹This chapter is based on "Coupling discharge and gas dynamics in streamer-less spark formation in supercritical N₂." by A. Agnihotri, W. Hundsdorfer and U. Ebert. *Japanese Journal of Applied Physics* 55, no. 7S2 (2016): 07LD06.

3.1 Introduction

Electrical breakdown and dielectric recovery are important issues in high-voltage switch gear. A common medium in gaseous insulation and high-voltage switching is SF₆ which is known to have excellent switching properties [27, 28, 29, 30]. But the downside is that SF₆ is an extreme green house gas with a global warming potential of 23 900 times that of CO₂. Supercritical liquids might be a replacement due to their high density, dielectric strength etc. [31, 32]. The electric breakdown in supercritical N₂ — at 80 bar and 300 K — has recently been studied experimentally and theoretically by Zhang *et al.* [14]. However, in their simulation studies of the breakdown of supercritical nitrogen between two planar electrodes only the transversal structure of the breakdown channel was resolved in an extremely simplified model for the electric discharge. We here study the breakdown process assuming that the breakdown channel is cylindrically symmetric, i.e., that we can treat the evolution in a radial and a longitudinal coordinate (r, z) .

Electric breakdown is typically assumed to evolve from initial electron avalanches through the space charge dominated streamer phase to a heat dominated leader or arc phase, and many experimental and theoretical studies have been performed [33, 34]. Space charge effects refer to the electric field enhancement at streamer head which supports the ionization reaction and thereby results in the subsequent breakdown of the medium [35, 24]. Here we demonstrate a different breakdown mechanism in short gaps with secondary emission from the cathode where a sequence of ionization waves and ion pulses heats the gas up until it breaks down.

To study this dynamics, we here develop a simulational code to study electrical breakdown where discharge and gas dynamics are coupled: the discharge generates ohmic heat that heats the gas. Consecutively the gas expands which changes the transport and reaction properties in the discharge.

Tholin *et al.* [36] studied the hydrodynamic expansion of the background gas after the voltage pulse. They assumed the reduced electric field E/N to be not affected by the changes in the background gas density, N , and hence do not solve the gas flow equations along with the discharge equations. This assumption is reasonable as the gas temperature does not rise rapidly during the short voltage pulse and hence the gas density is not much changed.

Komuro *et al.*, [37] solve the discharge equations and background gas flow equations simultaneously during the voltage pulse, but only on the electron timescale.

In this work, we solve the discharge equations and background gas flow equations simultaneously but now on the timescale of ion motion.

This paper is organized as follows: In Sect. 2 we introduce the notation and describe our model for the coupled system. Sect. 3 contains initial and boundary conditions and numerical algorithms. Sect. 4 is devoted to simulation results and

discussion. Finally, we summarize our finding and give an outlook in Sect. 5.

3.2 Description of the model

We develop a two-dimensional cylindrically symmetric code to carry out the simulations. The code components include a model for the electric discharge on the timescale of ion motion and a model for the background gas. The two models are coupled to study the interplay between the electric discharge and the background gas.

3.2.1 Model for the electric discharge

To describe the discharge dynamics, we adopt the first-order reaction-drift-diffusion model [38] in local field approximation for electrons and ions, coupled to Poisson's equation to calculate the electric field self-consistently. We focus on the timescale of ion motion and assume that the electrons are moving infinitely fast [39, 40]. This means that the electron density adapts to the ion density infinitely fast and the derivative $\partial_t n_e$ can be set to zero in an adiabatic decoupling procedure. Hence, our reaction-drift-diffusion equations become:

$$-\nabla \cdot (n_e \mu_e \mathbf{E} + D_e \nabla n_e) = S_e, \quad (3.1a)$$

$$\partial_t n_p + \nabla \cdot (n_p \mu_p \mathbf{E} - D_p \nabla n_p) = S_e, \quad (3.1b)$$

$$-\nabla^2 \phi = \frac{e}{\epsilon_0} (n_p - n_e), \quad (3.1c)$$

$$\mathbf{E} = -\nabla \phi. \quad (3.1d)$$

In the above equations, n_e and n_p denote the number density of electrons and positive ions, respectively, where we assume only one ion type N₂⁺ to be formed. \mathbf{E} represents the electric field, ϕ represents the electric potential and e is the elementary charge. The mobilities (and diffusion coefficients) of electrons and positive ions are denoted by μ_e (and D_e) and μ_p (and D_p), respectively; they are assumed to be functions of the reduced electric field E/N , where N is the gas number density. S_e is the impact ionization term in local field approximation.

The transport and reaction coefficients were taken from the work of Montijn *et al.* [24] and scaled to 80 bar.

At the cathode we implement secondary emission of electrons on ion impact, i. e.

$$n_e = \gamma n_p, \quad (3.2)$$

where γ is the secondary emission coefficient whose value is taken to be 0.07 for simplicity.

3.2.2 Model for the background gas

To describe the gas dynamics, we adopt the compressible Euler equations [41] without viscosity, as in the studies by Tholin *et al* [36, 42]. The source term for energy transfer from the electric discharge to the gas is Joule heating [36, 43, 44, 45]. The system is closed with the ideal gas law. The relevant equations in cylindrical coordinates are

$$\frac{\partial \rho}{\partial t} + \nabla \cdot (\rho \mathbf{v}) = 0, \quad (3.3a)$$

$$\frac{\partial (\rho v_z)}{\partial t} + \nabla \cdot (\rho v_z \mathbf{v}) = -\frac{\partial p}{\partial z}, \quad (3.3b)$$

$$\frac{\partial (\rho v_r)}{\partial t} + \nabla \cdot (\rho v_r \mathbf{v}) = -\frac{\partial p}{\partial r}, \quad (3.3c)$$

$$\frac{\partial \xi}{\partial t} + \nabla \cdot (\mathbf{v}(\xi + p)) = \eta e (\mathbf{j}_c \cdot \mathbf{E}), \quad (3.3d)$$

where \mathbf{j}_c is the conductive current density given by

$$\mathbf{j}_c = \mathbf{j}_e + \mathbf{j}_p, \quad (3.4)$$

where

$$\mathbf{j}_e = \mu_e n_e \mathbf{E} + D_e \nabla n_e, \quad (3.5a)$$

$$\mathbf{j}_p = \mu_p n_p \mathbf{E} - D_p \nabla n_p. \quad (3.5b)$$

Here ρ is the gas mass density, \mathbf{v} is the gas velocity, $\xi = \rho \epsilon + \frac{1}{2} \rho v^2$ is the total energy per unit volume, with ϵ being the internal energy per unit mass for the gas, p is pressure, and η is the fraction of discharge energy that contributes to gas heating. We have adopted the value of 0.3 for η as suggested by Tholin *et al.* [36] based on physical arguments and fitting with experiments.

3.2.3 Coupling between discharge and gas dynamics

The electric discharge generates the Joule heat $\eta e (\mathbf{j}_c \cdot \mathbf{E})$ in the model for the gas. When the temperature rises, the gas expands, the gas number density N decreases and hence the transport coefficients of the charged species and the reduced electric fields E/N increase. There is a feedback in both directions (from discharge to gas and back) at every time step of the evolution.

3.3 Simulation conditions

In this work we adopt 3D-cylindrical geometry with azimuthal symmetry around the discharge axis ($r = 0$). The electrode configuration is plane-to-plane. The background gas is taken to be supercritical N₂ at a temperature of 300 K and a pressure of 80 bar [14]. The applied electric field $\mathbf{E} = -E\hat{e}_z$ (where E is the magnitude of the electric field and \hat{e}_z is the unit vector in the z -direction) drives the system. The electrons therefore move in the positive z -direction and the positive ions in the negative z direction under the action of the field. The system length is $L = 0.3$ mm in z -direction and $3L$ in r -direction.

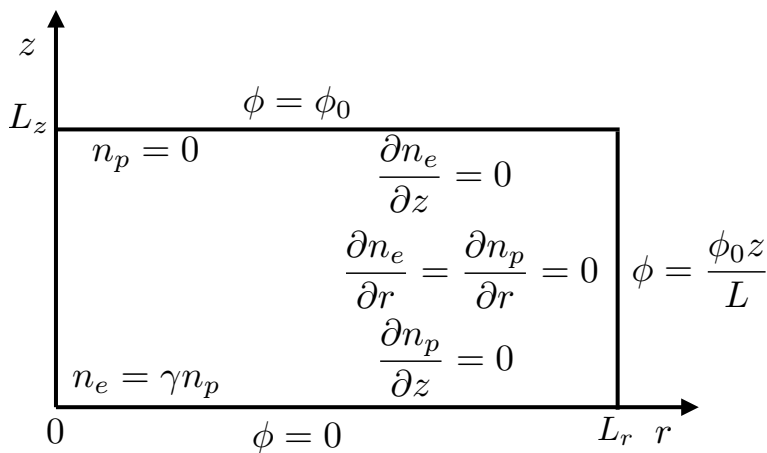


Figure 3.1: Simulation setup: In the above figure, the gas medium is supercritical N₂ at temperature of 300 K and pressure of 80 bar. The boundary conditions for charge densities (electronic/ionic) and for the electric potential are indicated. The gap length, L , is 0.3 mm and a dc-voltage, ϕ_0 of 54 kV is applied.

3.3.1 Boundary conditions

We have cylindrical symmetry around the discharge axis ($r = 0$).

We set a homogeneous Neumann boundary condition for electron/ion densities onto the boundary in the radial direction. On the top boundary, the anode, we set positive ion density equal to zero, as ions are only produced within the gap and drift downward. Also, we set the perpendicular component of diffusive flux of electrons on the top boundary to zero.

At the bottom electrode, the cathode, the perpendicular component of the ion-diffusive flux is set to zero. Also, since we include secondary electrode emission, the Dirichlet boundary condition (3.2) is imposed on the electron density

at the cathode. Figure 1 shows the implemented boundary conditions.

The electric potential is fixed as $\phi = 0$ or 54 kV on the lower ($z = 0$) or upper ($z = L$) electrode. The electric potential varies linearly with z on the right lateral boundary. In mathematical terms, the b.c. are

$$\frac{\partial n_e}{\partial z}(r, L_z, t) = 0, \quad n_e(r, 0, t) = \gamma n_p(r, 0, t), \quad \frac{\partial n_e}{\partial r}(L_r, z, t) = 0, \quad (3.6)$$

$$n_p(r, L_z, t) = 0, \quad \frac{\partial n_p}{\partial z}(r, 0, t) = 0, \quad \frac{\partial n_p}{\partial r}(L_r, z, t) = 0, \quad (3.7)$$

$$\phi(r, 0, t) = 0, \quad \phi(r, L_z, t) = \phi_0, \quad \phi(L_r, z, t) = \frac{\phi_0 z}{L_z}, \quad (3.8)$$

where $L_r = 3L$, $L_z = L$ and $\phi_0 = 54$ kV.

For the Euler equations, extrapolated boundary conditions[46, 47] were assumed on all boundaries.

3.3.2 Initial conditions

We start the simulation with a Gaussian distribution of ions and electrons

$$n(r, z)|_{t=0} = n_0 \exp \left[-\frac{r^2}{\sigma_r^2} - \frac{(z - z_0)^2}{\sigma_z^2} \right], \quad (3.9)$$

where we choose $n_0 = 5 \times 10^{11} \text{ cm}^{-3}$, $z_0 = 0.09 \text{ mm}$, $\sigma_r = 6.9 \text{ }\mu\text{m}$ and $\sigma_z = 27.6 \text{ }\mu\text{m}$. This seed amounts to about 3700 electrons and ions. The initial gas temperature and pressure are chosen to be 300 K and 80 bar, respectively. Also, the gas velocity is chosen to be zero at the beginning of the simulation.

3.3.3 Numerical method

The continuity equations of the discharge model are discretized with the MUSCL scheme [26, 48] using the Koren limiter function [22]. Since we expect large gas density gradients in the system, we implemented a high-resolution scheme which although being computationally expensive is good at handling large gradients. For time-integration, explicit second-order Runge-Kutta (midpoint rule) [49] is used. To solve Poisson's equation we used the FISHPACK solver [50]. Also, the Euler equations are discretized with the same numerical scheme as the discharge equations. A grid of 500 cells was taken along the z -axis and of 3×500 in the r -direction.

3.4 Results and discussion

We simulated the evolution of a discharge in nitrogen at 80 bar in a 0.3 mm gap with 54 kV applied, and with the initial seed (3.9) of about 3700 electrons and

ions. This seed might have been created by cosmic radiation or radioactivity [51], but the possible formation process is beyond the scope of the current simulations.

Figure 2 shows the evolution of electron density n_e , ion density n_p , reduced electric field E/N , ratio of gas density over initial gas density ρ/ρ_0 and gas temperature T . We now discuss the rows of the figures sequentially.

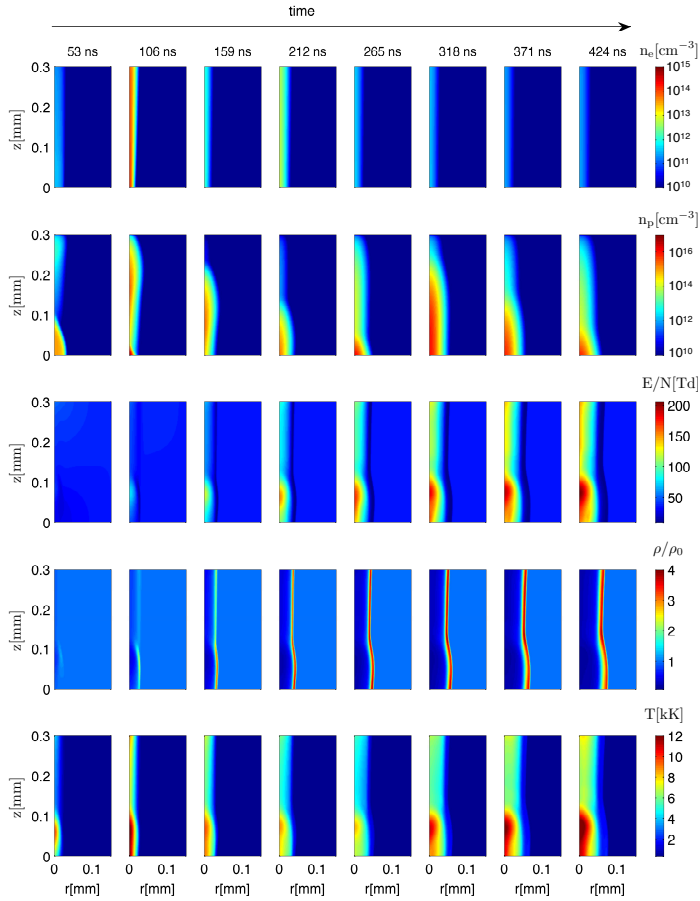


Figure 3.2: Evolution of electron number density n_e , ion number density n_p , reduced electric field E/N , gas density ρ/ρ_0 normalized to the density ρ_0 at $T = 300$ K and 80 bar, and gas temperature T . The initial seed of electrons and positive ions (3.9) is placed on the discharge axis ($r = 0$) at $z = 0.09$ mm. The gas is nitrogen at 80 bar, and 54 kV are applied to a gap of 0.3 mm.

n_e : The electrons move much faster than the ions, and they are created by secondary emission at the cathode below and by impact ionization when they move upwards; therefore the electron density near the cathode is proportional

to the local ion density and the growth of electron density in the z direction is determined by the impact ionization rate.

n_p : An ion is generated together with every electron, but the ions move down more slowly. The time for the ions to cross the gap in the initial gas density and electric field is 172 ns. When an ion wave reaches the cathode, new electrons are emitted and new ions and electrons are created in the gap. This refreshes the ion density and starts a new ion wave propagating downward.

E/N : An important observation is that the electric field never changes much, i.e., the charge densities of electrons and ions are not sufficient to seriously modify the background electric field. The changes in the reduced electric field E/N are due to the change of the gas density. In the last time step plotted at $t = 424$ ns, the reduced electric field reaches a maximum of about 200 Td, while the breakdown reduced electric field in air is 120 Td [52]. We expect that the electric breakdown will continue after such high reduced fields have been reached.

In air, the breakdown field is defined as the value of the electric field at which the generation rate of electrons equals the attachment rate. In our case we have considered pure nitrogen in which attachment is absent. As air consists of 80% nitrogen, in practice the breakdown field in air provides a reasonable scale.

ρ/ρ_0 and T : The temperature increases from 300 up to 12000 K mainly in the lower part of the system. Since the initial seed was located in the lower half, after the first time step the ions have drifted a little from their position but the electron density in the channel has been calculated all along the channel from (3.1a), starting from cathode. Electron density is essentially very small since the ions have not bombarded the cathode yet. Hence we see a concentration of heating at the position of the ions. This high temperature increases the pressure and creates an expansion shock front that can be seen in the density plot. At $t = 159$ ns, the gas temperature has dropped on the lower part of the axis. In other words, the gas has *cooled* down. This happens due to the radial movement of shock wave.

3.5 Summary and outlook

We have simulated the evolution of a coupled system on electric discharge and background gas in a short plane-to-plane electrode configuration in 2D-cylindrical symmetry. We have shown that with a simple model consisting of electron impact ionization and secondary electrode emission, simple relationships between the transport coefficients and gas density and heat transfer from the electric discharge to the gas, one can understand the formation of a spark. More specifically one can see how heat induced changes in the background gas density can trigger ionization in the discharge channel leading to breakdown. We see a pulsating behavior in the ion number density: the ions reach the cathode, liberate electrons from it and hence generate more electrons and ions in the gap. These ions propagate down to

the cathode. This pulsating cycle continues until either the temperature induced density changes drive the reduced electric field to values above breakdown, or until the discharge activity stops.

We emphasize that this slow heat driven breakdown mechanism of short gaps is basically different from the fast streamer breakdown mechanism that is driven by space charge effects at the streamer head.

The current model was developed with the motivation to understand electrical breakdown with a simple physical model. Of course, one can broaden the model by further improvements, particularly by incorporating the complex relationship between transport coefficients and the gas density, and by further investigating the effects of temperature on the electron-ion source terms. These improvements will be part of future work.

Chapter 4

Modeling heat dominated electric breakdown in air, with adaptivity to electron or ion time scales

We model heat dominated electrical breakdown in air in a short planar gap. We couple the discharge dynamics in fluid approximation with the hydrodynamic motion of the air heated by the discharge. To be computationally efficient, we derive a reduced model on the ion time scale, and we switch between the full model on the electron time scale and the reduced model. We observe an ion pulse reaching the cathode, releasing electrons by secondary emission, and these electrons create another ion pulse. These cycles of ion pulses might lead to electrical breakdown. This breakdown is driven by Ohmic heating, thermal shocks and induced pressure waves, rather than by the streamer mechanism of local field enhancement at the streamer tip.

1

¹This chapter is based on "Modeling heat dominated electric breakdown in air, with adaptivity to electron or ion time scales." by A. Agnihotri, W. Hundsdorfer and U. Ebert. *Plasma Sources Science and Technology* 26, no. 9 (2017): 095003.

4.1 Introduction

Gas heating in electrical discharges has a long research history. It has been studied in the context of fast gas heating [53, 54, 55, 56, 57], plasma-assisted combustion [58], atmospheric lightning [45] etc. On the one hand, increased temperature can change the chemical reaction rates in the discharge plasma. On the other hand, the thermal expansion of the gas can change the gas density and hence the reduced electric field in the inter-electrode gap. Both mechanisms can sustain spark formation [59, 60], and gas heating can also create turbulent flows [61]. In the present work, we concentrate on the effect of gas heating and expansion.

So far the majority of simulation studies pertaining to gas heating in atmospheric pressure discharges have been performed in a 0D or 1D spatial configuration in which the structure of discharge is rather homogeneous. Due to large difference in timescales of gas movement and electron dynamics, solving the two systems simultaneously becomes computationally very expensive. Recently, there has been progress in extending models to 2D (which is meant to mean 3D with cylindrical symmetry) which brings them closer to experiments and observations as the structure of a spark discharge is usually filamentary. Komuro and Ono [37] studied the mechanism of fast gas heating and the effects of humidity in atmospheric pressure streamer discharges. They solved the coupled system of electric discharge and gas simultaneously up to time $t = 3 \mu\text{s}$. Tholin and Bourdon [36] simulated the hydrodynamic expansion following a nanosecond pulsed discharge in air at STP. During the short pulse they approximated the gas density as constant, hence they did not need to solve the coupled system of electric discharge and gas simultaneously. Kacem *et al.* [62] simulated the expansion of thermal shock and pressure waves induced by streamer dynamics in positive DC corona discharges. They as well do not solve the full coupled system of electric discharge and gas dynamics. However, they do remark that direct coupling of the gas dynamics with the streamer simulation should be undertaken in order to better understand the effect of temperature increase and of the gas expansion on the development of successive discharges and on the electrical relaxation.

In the current paper, we simulate electrical breakdown in a short planar gap in 2D (r-z coordinates) with secondary electron emission where Ohmic heating promotes ionization growth, rather than the space charge dominated streamer breakdown mechanism. Initially only an avalanche without (streamer-type) space charge effects might have developed in a short undervolted gap, but the deposited Ohmic heat might eventually lead to electric breakdown. This is challenging to simulate as in the initial stage the electron dynamics has to be followed, and later on the much slower ion dynamics has to be resolved, and both have to be coupled to the hydrodynamics of the medium. We present a model on the time scale of ion motion, that is a reduced version of the full discharge dynamics, and with adaptivity in time, i.e., we switch between dynamical calculations on electron

and ion time scale as needed. In the present work, this is done manually, but we also discuss possible numerical switching criteria. The reduced model on the ion time scale was introduced in earlier work of Sijacic [40, 39] where it was applied to study the transition from Townsend to glow discharge.

We initiate the discharge closely below breakdown conditions, i.e., when the effective Townsend ionization coefficient α_{eff} is negative. As α_{eff} is a function of the reduced electric field, i.e., of electric field over gas density E/N , gas heating and subsequent expansion causes α_{eff} to grow, and might make it positive eventually. But that is not sufficient on time scales considerably longer than the time the ions need to cross the gap. On that time scale secondary emission from the cathode needs to sustain the discharge, and in a planar configuration with constant field and gas density, the discharge will grow further if

$$\gamma(e^{\alpha_{\text{eff}}d} - 1) > 1. \tag{4.1}$$

Here d is the distance between the electrodes and γ is the secondary electron emission coefficient which is the ratio of the number of emitted electrons over the number of ions impacting the cathode.

In our previous work [63], we developed and employed a similar 2D cylindrically symmetric model to study streamer-less spark formation in supercritical N_2 . A limitation of that model was that it computed the relevant physical quantities on the ion timescale only, not resolving the time scale of the electron motion. Therefore we missed some initial heating effects, as we discuss here in Section 3.

The paper is organized as follows. In Section 2 we introduce the mathematical model and notation for our coupled system of the electric discharge and the gas. In Section 3 we discuss the reduction of the full discharge model to a model on the ion time scale. We also compare results of the full model of the electrical discharge and of the reduced model in 1D, and we point out when the reduced model can be used to speed up simulations. In Section 4 we present and discuss the results of the 2D simulation of the electric discharge in plane-to-plane geometry in air at standard temperature and pressure. Finally, in Section 5 we summarize our findings and present an outlook.

4.2 Model formulation

We study how a pulsed electric discharge is coupled to the dynamics of the background gas due to the deposited Ohmic heat and thermal expansion. Therefore the model is composed of two components, one for the dynamics of electrons and ions in the electric discharge and one for the dynamics of the background gas.

4.2.1 Model for the electric discharge dynamics

To describe the discharge dynamics, we adopt the classical first-order drift-diffusion-reaction model [38] in local field approximation for electrons and posi-

tive and negative ions, coupled with Poisson's equation to self-consistently compute the electric field:

$$\partial_t n_e + \nabla \cdot \mathbf{j}_e = S_e, \quad \mathbf{j}_e = -\mu_e \mathbf{E} n_e - D_e \nabla n_e + \mathbf{v} n_e \quad (4.2)$$

$$\begin{aligned} \partial_t n_i + \nabla \cdot \mathbf{j}_i = S_i, \quad \mathbf{j}_i = \sigma_i \mu_i \mathbf{E} n_i - D_i \nabla n_i + \mathbf{v} n_i \\ \text{for ion species } i = 1, \dots \end{aligned} \quad (4.3)$$

$$\nabla^2 \phi = -\frac{e}{\epsilon_0} \left(-n_e + \sum_i \sigma_i n_i \right), \quad \mathbf{E} = -\nabla \phi. \quad (4.4)$$

Here the lower index e labels the electrons and $i = 1, \dots$ the different types of positive and negative ions. Further, $n_{e,i}$ is the number density of the charged species, $\mathbf{j}_{e,i}$ their particle current density, $\mu_{e,i}$ and $D_{e,i}$ their mobility and diffusion coefficients, and $\sigma_i = \pm 1$ their polarity. (Note that the electric current density carried by particle type i is $e\sigma_i \mathbf{j}_i$.) ϕ denotes the electric potential, \mathbf{E} denotes the electric field. e is the elementary charge and ϵ_0 denotes the permittivity of vacuum. Finally, \mathbf{v} is the velocity of the neutral gas through which the charged particles are moving; as the degree of ionization of the gas molecules stays below 10^{-8} in the presented simulations until the final stages, the neutral gas molecules provide the rest frame for the motion of the charged particles.

S_i is the source term for the ion species with label i . For electrons in attaching gases like air at standard temperature and pressure we have

$$S_e = (\alpha - \eta) \mu_e E n_e = \alpha_{\text{eff}} \mu_e E n_e, \quad (4.5)$$

where α accounts for electron impact ionization and η for attachment, and $\alpha_{\text{eff}} = \alpha - \eta$ is the effective Townsend ionization coefficient. Here recombination or dissociative attachment or detachment are neglected to keep the notation simple, but they can easily be introduced for different gases. Similarly the method of time adaptivity introduced in the next section is not limited to the local field approximation or to the drift-diffusion-reaction model.

Finally, the discharge couples to the gas dynamics through the gas velocity \mathbf{v} , and because transport and reaction coefficients μ_i , D_i and α depend on the reduced electric field E/N . Here N is the number density of neutral gas molecules; it is related to the mass density ρ as $\rho = m_w N$, where m_w is the mass of the gas molecule.

4.2.2 Boundary conditions for the discharge

We assume a short discharge gap between planar electrodes. To sustain the discharge, we include secondary emission of electrons from the cathode on impact of positive ions. This is implemented as a Dirichlet boundary condition for the electron density n_e

$$\mu_e n_e = \gamma \sum_j \mu_j n_j \text{ on the cathode.} \quad (4.6)$$

Here n_j is the number density of the positive ion species j reaching the cathode. Furthermore, we assume that the density of positive ions vanishes on the anode and has a homogeneous Neumann boundary condition on the cathode

$$n_j = 0 \quad \text{on the anode,} \quad (4.7)$$

$$\partial_n n_j = 0 \quad \text{on the cathode,} \quad (4.8)$$

where ∂_n denotes the spatial derivative normal to the electrode surface. For negative ions, the role of anode and cathode are exchanged.

We remark that when the full model of electric discharge is used for computation of electron density, two boundary conditions are required. For that we implement a homogeneous Neumann boundary condition on electron density on the anode

$$\partial_n n_e = 0 \quad \text{on the anode.} \quad (4.9)$$

At the lateral boundaries, we implement homogenous Neumann boundary condition for the charge densities,

$$\partial_r n_{e,i}|_{r=0} = \partial_r n_{e,i}|_{r=L_r} = 0. \quad (4.10)$$

The lateral boundary ($r = L_r$) of the computational domain extends far from the discharge axis ($r = 0$) so that the boundary effects do not interfere with the dynamics and give rise to unphysical solutions.

4.2.3 Model for the gas dynamics

To model the gas dynamics, we adopt the compressible Euler equations without viscosity. The relevant equations for the conservation of mass, momentum and energy are in cylindrical coordinates

$$\frac{\partial \rho}{\partial t} + \nabla \cdot (\rho \mathbf{v}) = 0, \quad (4.11)$$

$$\frac{\partial (\rho v_r)}{\partial t} + \nabla \cdot (\rho v_r \mathbf{v}) = -\frac{\partial p}{\partial r}, \quad (4.12)$$

$$\frac{\partial (\rho v_z)}{\partial t} + \nabla \cdot (\rho v_z \mathbf{v}) = -\frac{\partial p}{\partial z}, \quad (4.13)$$

$$\frac{\partial \xi}{\partial t} + \nabla \cdot (\mathbf{v}(\xi + p)) = S_\xi, \quad (4.14)$$

with $\mathbf{v} = (v_r, v_z)$ and $\nabla = (\partial_r, \partial_z)$. Here ρ is the gas mass density, \mathbf{v} the gas velocity, p is gas pressure, and

$$\xi = \rho \epsilon + \frac{1}{2} \rho v^2 \quad (4.15)$$

is the total energy per unit volume. ϵ is the internal energy per unit mass; it is related to pressure through the ideal gas law

$$p = \rho \epsilon (\Gamma - 1), \quad (4.16)$$

where Γ is the heat capacity ratio for the background gas whose value we assume to be constant and equal to 1.4 for air. We remark that the heat capacity will increase at the high temperatures reached at the final stages of the presented simulations, but this effect is here not taken into account.

We note that in principle the electron and ion drag force would need to be included in the momentum balance of equations (4.12) and (4.13), but we neglect it as ionization density in the present simulations is too low.

S_ξ is the energy source term that models gas heating. It is modeled as follows: The electrical power density deposited by the discharge is

$$P = e \mathbf{E} \cdot \left(-\mathbf{j}_e + \sum_i \sigma_i \mathbf{j}_i \right), \quad (4.17)$$

where $\mathbf{j}_{i,e}$ is the particle current density of the charged species with label i or of the electrons e . We assume that a fraction η of the power density P is converted immediately (on a nanosecond time scale) into heat ξ [55, 36], and the remaining $(1 - \eta)$ of P is first stored in vibrational states of the molecules in an energy density reservoir ϵ_v and released as heat with a relaxation time τ . This process is modeled as

$$\frac{\partial \epsilon_v}{\partial t} = (1 - \eta) P - \frac{\epsilon_v}{\tau}, \quad (4.18)$$

$$S_\xi = \eta P + \frac{\epsilon_v}{\tau}. \quad (4.19)$$

Equation (4.18) for ϵ_v can be integrated which leads to the final expression for S_ξ

$$S_\xi(\mathbf{r}, t) = \eta P(\mathbf{r}, t) + (1 - \eta) \int_{-\infty}^t P(\mathbf{r}, t') e^{-(t-t')/\tau} \frac{dt'}{\tau}. \quad (4.20)$$

Throughout the simulations presented here, we use $\eta = 0.15$ and $\tau = 20 \mu\text{s}$. The values of these parameters are discussed in Section 4.2.1.

4.2.4 Boundary conditions for the fluid equations

For the fluid equations describing gas flow, we implement the following boundary conditions on the electrodes ($z = 0$ and $z = L_z$)

$$v_z = 0, \quad (4.21)$$

$$\partial_z p = 0. \quad (4.22)$$

On the outer radial boundary ($r = L_r$) of the computational domain, we implement an outflow boundary condition. These are not *physical* boundary conditions, but they are implemented for computation. The details of the implementation are discussed in Appendix A. 4. We remark that for the time simulated in this work, the shockwaves travelling in the radially outward direction do not reach the outer boundary.

4.3 The reduced model on the ion time scale and time adaptivity to electron or ion dynamics

4.3.1 Motivation and problem statement

At the beginning of a pulsed discharge in a short gap, free electrons might deposit energy in the gas while drifting through the system. This is the avalanche and possibly the streamer phase, dominated by electron dynamics while the ions hardly move. At later stages, the dynamics might be dominated by the ions that move much more slowly due to their higher mass; also the heat driven expansion of the carrier gas evolves on a much longer time scale than the electron dynamics. During this stage, the electrons might form an approximately stationary distribution determined by the local electric field and gas density. But it is also possible — as we will see below —, that one needs to switch back to the time scale of electron motion.

Solving the long time evolution completely on the electron time scale requires very long computation times. Therefore we here develop a method that is adaptive in time, switching between the time scales of electron or ion dynamics. In subsection 4.3.2 we extend the method of adiabatic decoupling [40, 39] to discharges with multiple ion species, thus deriving a reduced model on the time scale of ion motion. Then we test numerically in subsection 4.3.3 when the reduced model on the ion time scale is an appropriate approximation of the full dynamics. Finally in subsection 4.3.4, we briefly discuss criteria for switching between the full and the reduced model.

4.3.2 Derivation of the reduced model on the ion time scale

The discharge model introduced in the last section accounts for the electron time scale. However, eventually the discharge dynamics might be dominated by the ion dynamics while the much faster electrons can approach an approximately stationary distribution around the ions. And when the same number of electrons and ions are created locally, but the electrons move much faster, the space charge density is dominated by the ions. This is even more true when electron loss by attachment is included.

The derivation of an appropriate model can be formalized by methods for differential equations such as rescaling and singular perturbation theory. These methods identify which terms in an equation balance each other to form the solution, and which terms can be neglected. This balance of terms can change depending on conditions, both in space and in time. We introduced the method in [40, 39] under the name “adiabatic decoupling” as it was called in early quantum mechanics to study electron dynamics in atoms and molecules where the nuclei are much heavier and slower than the electrons. In [40, 39] the discharge model on the ion time scale was derived for only one ion species, and assuming

that mobilities and diffusion coefficients are constant. Here we generalize the derivation to several ion species and to transport coefficients depending on the local reduced field E/N or other local variables.

As the basic parameter for the rescaling, we choose mobilities μ_e^0 and μ_1^0 of the electrons and of the dominant positive ion species for some characteristic, but arbitrary value of the reduced electric field E/N . Their ratio determines the small parameter

$$\mu = \frac{\mu_1^0}{\mu_e^0} \ll 1. \quad (4.23)$$

Mobilities and diffusion coefficients of the ions are now rewritten as

$$\frac{\mu_i(E/N)}{\mu_e^0} = \mu f_i(E/N), \quad \frac{D_i(E/N)}{D_e^0} = \mu g_i(E/N), \quad (4.24)$$

where the functions f_i and g_i are of order unity, and where D_e^0 is the electron diffusion coefficient at the same characteristic electric field as μ_e^0 . This notation makes explicit which terms in the equations are of order $\mu \ll 1$ or of order unity. Furthermore, we assume the gas velocity \mathbf{v} to be of the order of a typical ion drift velocity or smaller, i.e.,

$$\mathbf{v} = \mu \tilde{\mathbf{v}}, \quad |\tilde{\mathbf{v}}| \leq \mathcal{O}(\mu_1 |\mathbf{E}|). \quad (4.25)$$

Now when these relations are inserted into the discharge model (4.2)–(4.4) and when the limit $\mu \rightarrow 0$ is taken, all ion currents and the gas velocity vanish, and one recovers the well known avalanche and streamer discharge model that traces the electron motion and neglects the ion motion:

$$\partial_t n_e + \nabla \cdot (-\mu_e \mathbf{E} n_e - D_e \nabla n_e) = S_e, \quad (4.26)$$

$$\partial_t n_i = S_i \text{ for ion species } i = 1, \dots \quad (4.27)$$

$$\nabla^2 \phi = -\frac{e}{\epsilon_0} \left(-n_e + \sum_i \sigma_i n_i \right), \quad \mathbf{E} = -\nabla \phi. \quad (4.28)$$

But in a singularly perturbed set of differential equations it happens typically, that also another scaling can be chosen. When we focus on the situation where electrons and ions are created in equal rates in time, but move with different velocities, their current densities should be similar: $\mu_e n_e = \mathcal{O}(\mu_1 n_1)$. This suggests to scale the electron density as

$$\tilde{n}_e = \frac{n_e}{\mu}; \quad (4.29)$$

as \tilde{n}_e and n_i are of the same order of magnitude.

Furthermore the time is rescaled to focus on the ion motion:

$$\tilde{t} = \mu t. \quad (4.30)$$

Substituting these identities into the discharge model and using (4.25), we find

$$\mu \frac{\partial \tilde{n}_e}{\partial \tilde{t}} + \nabla \cdot (-\mu_e \mathbf{E} \tilde{n}_e - D_e \nabla \tilde{n}_e + \mu \tilde{\mathbf{v}} \tilde{n}_e) = (\alpha - \eta) \mu_e E \tilde{n}_e, \quad (4.31)$$

$$\frac{\partial n_1}{\partial \tilde{t}} + \nabla \cdot (\mu_e^0 f_1 \mathbf{E} n_1 - D_e^0 g_1 \nabla n_1 + \tilde{\mathbf{v}} n_1) = \alpha \mu_e E \tilde{n}_e, \quad (4.32)$$

$$\frac{\partial n_i}{\partial \tilde{t}} + \nabla \cdot (\sigma_i \mu_e^0 f_i \mathbf{E} n_i - D_e^0 g_i \nabla n_i + \tilde{\mathbf{v}} n_i) = \tilde{S}_i, \quad \tilde{S}_i = S_i / \mu, \\ \text{for ions } i = 2, \dots, \quad (4.33)$$

$$\nabla^2 \phi = -\frac{e}{\epsilon_0} \left(-\mu \tilde{n}_e + \sum_{\text{ions } i} \sigma_i n_i \right), \quad \mathbf{E} = -\nabla \phi. \quad (4.34)$$

Now the small parameter μ again appears explicitly as a linear coefficient of $\partial_{\tilde{t}} \tilde{n}_e$, of $\tilde{\mathbf{v}} \tilde{n}_e$ and of \tilde{n}_e in the Poisson equation. Here μ acts as a singular perturbation as it multiplies the time derivative $\partial_{\tilde{t}} \tilde{n}_e$. Letting $\mu \rightarrow 0$ defines the model on the ion time scale. After the rescaling is undone, the discharge model on the ion time scale is finally

$$\nabla \cdot (-\mu_e \mathbf{E} n_e - D_e \nabla n_e) = (\alpha - \eta) \mu_e E n_e, \quad (4.35)$$

$$\partial_t n_1 + \nabla \cdot (\mu_1 \mathbf{E} n_1 - D_1 \nabla n_1 + \mathbf{v} n_1) = \alpha \mu_e E n_e, \quad (4.36)$$

$$\partial_t n_i + \nabla \cdot (\sigma_i \mu_i \mathbf{E} n_i - D_i \nabla n_i + \mathbf{v} n_i) = S_i \text{ for ions } i = 2, \dots, \quad (4.37)$$

$$\nabla^2 \phi = -\frac{e}{\epsilon_0} \sum_{\text{ions } i} \sigma_i n_i, \quad \mathbf{E} = -\nabla \phi. \quad (4.38)$$

In contrast to the original model, the time derivative of the electron density and its coupling to the gas motion has disappeared, and the electron density is also eliminated from the Poisson equation. While this is the mathematical derivation of this limit, we discussed the physical justification for the approximation at the beginning of this section.

4.3.3 Numerical test of the reduced model on the ion time scale

We now have derived 2 different limits of $\mu \rightarrow 0$ for the discharge model, one in equations (4.26)–(4.28) on the electron time scale, and one in equations (4.35)–(4.38) on the ion time scale. In analytical approaches, such equations can be linked through asymptotic matching. In section 4 we will use these different models to perform numerical time integration that is adaptive to the state of the dynamics.

But here we will first test whether and when the reduced model on the ion time scale (4.35)–(4.38) approximates the full reaction drift diffusion model (4.2)–(4.4) well.

Simulation conditions.

In order to run simulations of the full model on the electron time scale up to $2 \mu\text{s}$ within reasonable computing times, we perform simulations in one spatial dimension. We model N_2 at standard temperature and pressure with two charged species, namely electrons and N_2^+ ions. The values of transport and reaction coefficients are taken from Montijn *et al.* [24]. We neglect electron diffusion in the reduced model. The gas gap between two planar electrodes has a length of $L = 0.46 \text{ mm}$, and we assume secondary emission from the cathode (4.6) with $\gamma = 0.07$. The electric potential difference between the electrodes is fixed in such a manner that the average electric field is 17 kV/cm , i.e., well below the breakdown value. The initial condition is a rectangular neutral seed with

$$n_e = n_+ = 4.8 \times 10^8 \text{ cm}^{-3} \text{ for } 0.5 L \leq x \leq 0.7 L. \quad (4.39)$$

The full model and the model on the ion time scale are spatially discretized using the schemes described in the Appendix A. For the spatial grid we choose 800 points which corresponds to a spatial resolution of $0.57 \mu\text{m}$. For time-stepping we use the explicit trapezoidal rule for both models. We verified that further refinement of the grid did not alter the results. Therefore numerical errors are insignificant in the presented results.

Comparison of results.

Figure 4.1 shows the spatial profiles of the electron number density $n_e(x, t)$, of the ion number density $n_+(x, t)$, and of the deposited energy density $\int_0^t P(x, \tau) d\tau$ (with the power density P of equation (4.17)) for different time steps. The blue lines indicate results of the full drift-diffusion-reaction model, and the red dotted line of the reduced model.

As the hydrodynamics of the gas is not followed here, the deposited energy density is determined by the discharge evolution, but does not couple back onto the discharge dynamics. The energy is included in our plots, because it shows characteristic differences between the models, that will be important for the solution of the full problem.

Let us start with discussing the full model indicated in blue.

- Initially at time $t = 0$ electron and ion density are identical and no energy is deposited yet. Up to time $t \approx 7 \text{ ns}$, the electrons drift out of the system while the ions do not move much. The electrons deposit energy along their drift trajectory as indicated in the right column. They also create additional electrons and ions by impact ionization along their path, but at such a low density that they are not visible on the plotted scale (except at the very last time step of $2 \mu\text{s}$).
- During the next larger time steps from 100 to 500 ns, the ions drift to the right while the electron density is negligible. After time $t = 500 \text{ ns}$ the ions hit the cathode and generate electrons by secondary emission. Therefore at time

$t = 750$ ns while the ions keep arriving at the cathode, the electron density has increased to a value of the order of 10^5 cm^{-3} . It decreases again after $t = 1$ μs when the ions have left the system. Note that the total energy density deposited after the primary electron and ion packages have left the system, is constant in space. This is correct and can serve as a consistency check, as the same number of electrons and ions have moved over each point in space, and as the electric field is constant.

- At the last time step $t = 2$ μs , two plateaus of ion density can be seen when the plot scale is changed from $5 \cdot 10^8/\text{cm}^3$ to $2 \cdot 10^5/\text{cm}^3$. As the ions move through the whole length of the system in about 2 μs , the higher plateau of ion density near the right boundary must have been created while the initial electron pulse moved out of the system up to time $t = 10$ ns. The second lower plateau that extends until about the middle of the system, must have been created when the initial ion pulse hit the cathode, during the time interval of 600 ns to 1 μs . The cycle of arriving ion packages of decreasing amplitude continues until the gap is devoid of ions and the discharge decays.

The reduced model on the ion time scale is indicated in red. The first observation is that the ion motion of the reduced model agrees with the one of the full model for almost all times. But there are important differences in the electron density and the deposited energy:

1. Initially up to time $t = 10$ ns, the electron density does not move out of the system, but disappears instantaneously in the first numerical time step. This is because the electron dynamics is not followed, but the electron density is determined by the electron density on the cathode together with the instantaneous equation (4.35). An immediate consequence is that these electrons do not deposit energy in the system during the initial stage, and this lack of energy is seen very clearly until the last time step of the simulation. This difference has an impact on the solution, if the gas dynamics due to heating couples back onto the discharge model.
2. At later times, the electron density is approximated very well by the reduced model, as zooming into a narrow range of values of the electron density at times $t = 750$ ns and $t = 2$ μs shows. However, there is a major discrepancy at time $t = 1$ μs . This is because at this time the ion density on the cathode and therefore the rate of electron injection into the system changes so rapidly, that the adiabatic elimination of the electron dynamics is not valid anymore.
3. At time $t = 2$ μs , the ion density approximated by the reduced and the full model differ significantly close to the cathode. The staircase structure predicted by the full model in the region $x \in (0.4$ mm, 0.48 mm) represents the ions that were created by the initial seed of electrons via impact ionization while drifting out of the system. However, in the reduced model the initial seed of electrons did not create any ions in the gap (see point 1 above).

4.3. The reduced model on the ion time scale and time adaptivity to electron or ion dynamics

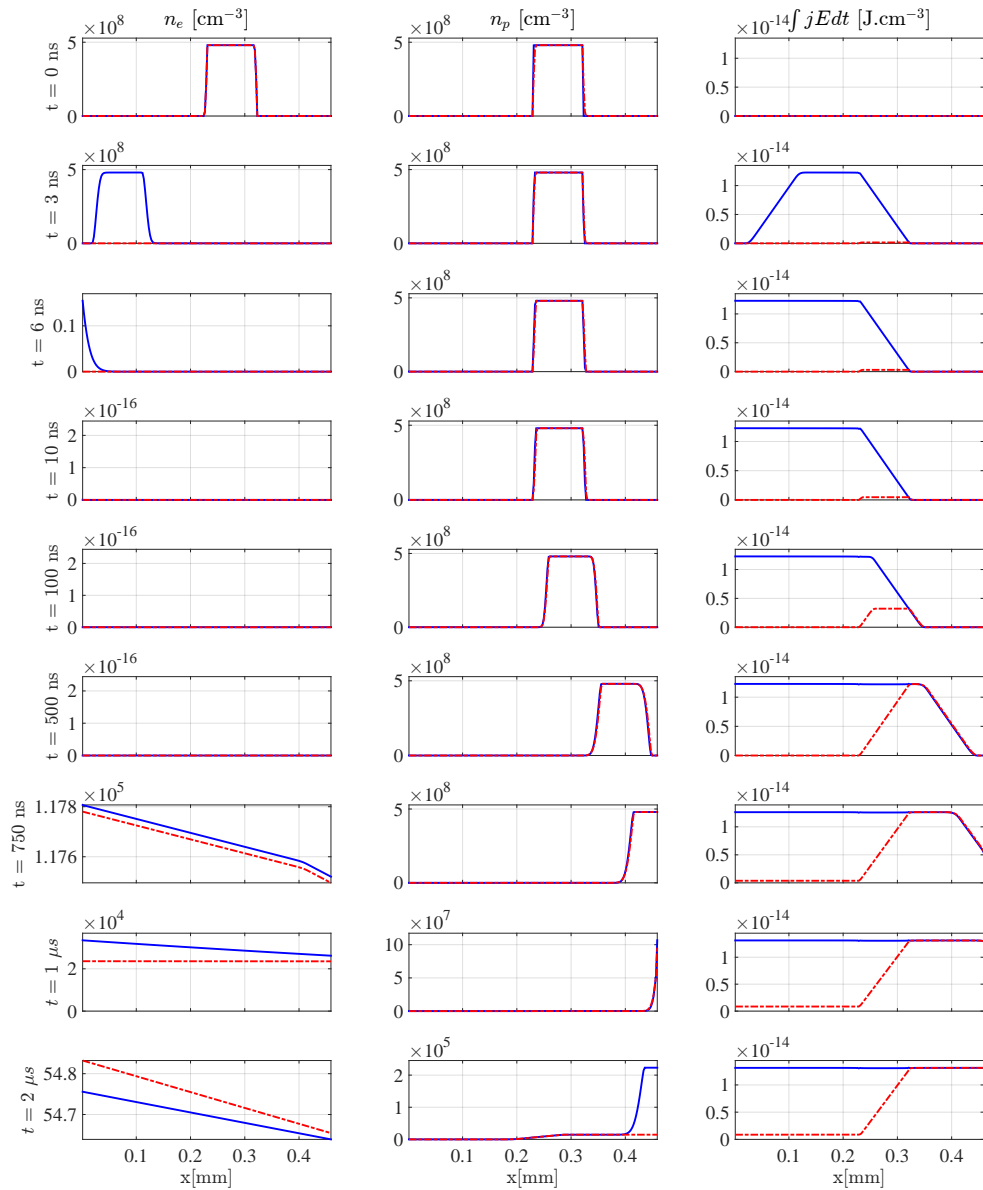


Figure 4.1: From left to right: Spatial profiles of electron number density n_e , ion number density n_+ and deposited electrical energy density for the 1D test case in nitrogen at standard temperature and pressure. The rows from top to bottom show the times 0, 3, 6, 10, 100, 500, 750, 1000, and 2000 ns. The results of the complete drift-diffusion-reaction model are drawn in blue, and those of the reduced model in red.

4.3.4 Computational adaptivity to electron or ion time scale

The observations above show that most of the time, the reduced model on the ion time scale approximates the full dynamics very well. Only during the time interval of the initial 8 ns, and during a short time interval around 1 μ s, the full dynamics differs from the reduced one. With an appropriate criterion the calculations can switch between the full and the reduced model and save substantial computing time.

We recall that in the reduced model the temporal derivative of the electron density $\partial_t n_e$ in (4.2) and the space charge effects of the electron density in (4.4) are neglected. In the present paper, the models are switched by hand, but we here briefly discuss possible programmed criteria that would allow the model to be adaptive in time.

For switching from the full to the reduced model, the size of $\partial_t n_e$ and n_e relative to the other terms in equations (4.2) and (4.4) can be taken as a criterion. For switching from the reduced to the full model, $\partial_t n_e$ is not available, but the effective change of n_e (due to changing distributions of ions, fields or gas density) within a numerical time step can be taken as a criterion. We will test the concept and develop a numerical algorithm for adaptivity in time in future work.

4.4 Simulation and results

4.4.1 Set-up of the model

We now present simulations of the evolution of an electric discharge in air at a pressure of 1 bar and a temperature of 300 K. The gap size of 1.38 mm, and the applied voltage 3.7 kV, which amounts to an electric field of 27 kV/cm as long as space charge effects of the discharge can be neglected. In such as field below breakdown, an electrical discharge can develop only due to field enhancement at the tip of a streamer discharge [35] or due to a (local) decrease of air density. In the simulations presented here, the decreasing air density drives the discharge evolution.

On the cathode, secondary emission (4.6) is included with a factor of $\gamma = 0.3$ which means that 10 positive ions impacting on the cathode liberate 3 electrons on average from the surface into the discharge. A self-sustained Townsend discharge can develop and grow in a homogeneous field E in a gas density N , if $\alpha_{\text{eff}}(E/N) \geq 1060/\text{m}$, according to (4.1).

To start the simulation, we place a seed of positive ions and electrons with a gaussian distribution given by

$$n(r, z)|_{t=0} = n_0 \exp \left[-\frac{r^2}{\sigma_r^2} - \frac{(z - z_0)^2}{\sigma_z^2} \right], \quad (4.40)$$

where we assign $n_0 = 14.4 \times 10^{11} \text{ cm}^{-3}$, $z_0 = 0.69 \text{ mm}$ and $\sigma_r = \sigma_z = 23 \text{ }\mu\text{m}$. This amounts to approximately 4.6×10^4 electrons and ions. Since we carry out our simulations in air, the ratio of the initial number density of positive nitrogen ions to the initial number density of positive oxygen ions is taken as 4:1. The initial velocity \mathbf{v} of the background gas is set equal to zero.

We perform the simulation in 3D with cylindrical symmetry around the z -axis (effectively 2D in r, z coordinates). In the radial direction the domain extends from $r = 0 \text{ mm}$ to $r = 4.14 \text{ mm}$. The ionic species included are N_2^+ , O_2^+ and O_2^- . As in section 3, we neglect electron diffusion in the reduced model. However, ion diffusion is taken into account in both the full model and the reduced model. The transport and reaction coefficients were read from a data file which was generated from online calculation tool BOLSIG+ (dated 27-06-2016) with the Phelps database [64, 65] from the LXCat website. The applied field is slightly below the breakdown value of 27.5 kV/cm at standard temperature and pressure, and therefore the effective ionization coefficient α_{eff} is negative. In the current work, we have not considered detachment processes. It will be included in our future work where chemical pathways will be treated more comprehensively.

For details regarding the numerical implementation of the schemes used in the computation of physical quantities related to electrical discharge and gas, we refer the reader to Appendix A.

We switch from the full model to the reduced model at time $t = 10 \text{ ns}$ to accelerate the computation. At this moment of time the primary electrons have left

the system and the system comprises of heavier ionic species. Furthermore, the contribution to the space charge is dominated by the ionic species and therefore the electric field profile is well approximated by the ionic distribution.

4.4.2 Simulation results

Figures 4.2 and 4.3 show the time evolution of electron density n_e , density n_p of positive oxygen and nitrogen ions, density $n_{\text{O}_2^-}$ of negative oxygen ions, effective Townsend coefficient $\alpha_{\text{eff}}(E/N)$, air temperature T and ratio ρ/ρ_0 of air density ρ over air density ρ_0 at standard temperature and pressure. In Figure 4.4 we plot temporal evolution of charge densities, gas temperature, gas pressure and relative gas density at the points $z = 0.3L_z$ (lower-half) and $z = 0.7L_z$ (upper-half) at time steps $t = 0 \mu\text{s}, 0.29 \mu\text{s}, 0.58 \mu\text{s}, 0.86 \mu\text{s}, 1.15 \mu\text{s}, 1.44 \mu\text{s}, 1.72 \mu\text{s}, 2.01 \mu\text{s}, 2.29 \mu\text{s}, 2.58 \mu\text{s}, 2.86 \mu\text{s}, 3.15 \mu\text{s}, 4.29 \mu\text{s}, 11.4 \mu\text{s}$ and $25 \mu\text{s}$. As the system evolves, we first observe activity in the upper-half due to the relatively fast movement of electrons. On the longer timescale activity in the lower half is observed when the ions move. The figures 4.2 and 4.3 show the full gap between the electrodes, but they zoom in into the structures near the center and don't show the full radial extension of the simulation. The temporal evolution is organized in three groups, where each group uses the same color scheme for densities and fields.

The figures show the following distinct stages of evolution:

Drift of the initial electrons to the anode up to time ≈ 7 ns:

The simulation starts with a concentrated ionization seed with an equal number of electrons and positive ions, while there are no negative ions in the system. Electric field, temperature and air density are constant in space. The Townsend coefficient α_{eff} is constant and negative.

Up to approximately 7 ns, the electrons drift upwards towards the anode and leave the system, while the positive ions are essentially immobile. While the electrons are drifting, their number decreases due to attachment and increases due to impact ionization; whether this relates to a net loss or a net gain, depends on the sign of α_{eff} . The electron attachment can directly be seen in the form of negative ions left behind along the electron trail. Due to the high value of the reduced electric field E/N , the attachment is quite strong and hence the number of negative oxygen ions quite large.

The electrons also generate Ohmic heat along their trail. This causes the local temperature T to rise up to a maximum of 500 K after 10 ns. As we assume that only 15% of the Ohmic heat is released directly, while 85% is stored in vibrational states and released as heat on a time scale of $20 \mu\text{s}$, the local temperature increases further up to a maximum of 720 K at time 293 ns. On the other hand, the time is too short for thermal expansion of the air, so the air

density N or ρ changes by approximately 1 %. The assumption of $\eta(E/N) = 15\%$ is based on previous work [55, 66]. Furthermore, in this work the ultrafast VT-relaxation timescale of the vibrationally excited $N_2(\nu)$ is treated as a parameter. We chose its value to be 20 μs . It was a choice based on work by Komuro *et al.* [67]

The effective Townsend coefficient α_{eff} depends on the reduced electric field E/N ; it is mostly negative, but reaches positive values above the electron package and below the ion package. As air density N has hardly changed, this indicates a local enhancement of the field E due to the local space charges.

Switching from full to reduced model at time 10 ns:

The numerical test of the last section has shown that the electrons have to be traced with the full dynamics during the initial stage. Otherwise no heat would be deposited during this stage, and also the trail of negative ions would be missing. After the initial electrons have left the system, we switch to the reduced model at time $t = 10$ ns for the rest of the simulation.

We mention that in previous work [63] we have started right away with the reduced model in a study of electric breakdown in supercritical nitrogen and therefore missed the heat deposited during the initial stage and its effects on the further dynamics.

Drift of the initial ions to the cathode up to time 1.7 μs :

The positive ions are initially inserted in the middle of the gap. In the initial air density and electric field they would reach the electrode after approximately 1.7 μs . And this is what they do, despite some field enhancement and decrease of air density. The trail of negative ions moves upwards towards the anode within the same time. As there is no source of electrons, the electron density vanishes after the initial electrons have reached the anode.

While the ions move, they deposit Ohmic heat. In the time frame $t = 0 - 293$ ns the heat deposited in the upper part of the system is significantly greater than in the lower part of the system. This occurs because in that time frame the ions have not drifted much and hence have not deposited substantial heat. In comparison, the electrons move rapidly and deposit electrical energy as heat while creating more electrons (and ions) on their way out. On the longer timescale the ions start drifting and deposit heat in the lower part of the system. This can be observed in the gas temperature profile on longer timescale where the temperature rises as the ions drift downward. Furthermore, the density of the positive ions also decreases due to radial diffusion as they drift downward.

The increased air temperature drives an expansion wave; hence the air density ρ decreases by up to 3 % in the center and increases by up to 2 % in the expansion shock wave. The change of N or $\rho = m_w N$ also leads to a change of the effective

Townsend coefficient α_{eff} .

Second and third ionization wave and electric breakdown due to heating:

At time $t = 1.72 \mu\text{s}$, the positive ions reach the cathode and liberate electrons through secondary emission. These electrons on their way up to the anode create ionization along their trail. In the plot at time $1.72 \mu\text{s}$, this can only be seen in the electron density. But at time $2.01 \mu\text{s}$, when the primary ions have left the system, the color coding of the ion density in the figure is changed, and two structures of positive ion columns are visible. The "blue" column (corresponding to a density of $\approx 5 \cdot 10^9/\text{cm}^3$) over almost the whole height of the system is the positive ion density created at that instance by the electrons. The negative ion density shows a corresponding column due to electron attachment along their trail. The "red" column (corresponding to a density of positive ions of $\approx 2.5 \cdot 10^{10}/\text{cm}^3$) in the lower half of the plot is the ion density created while the primary electrons drifted out of the system. This column in the mean time has drifted down by half the gap length.

Each column of positive ions will create another ionization wave when reaching the cathode, so the cycle repeats, but the amplitude decreases because the field is below breakdown, similarly to the 1D case discussed in the previous section. The difference lies in the fact that now air heating and expansion is included. The temperature keeps increasing in the channel and drives an expansion shock wave where the air density increases by 30 %, while it decreases in the channel by 50 % at time $25 \mu\text{s}$. This leads to a large increase of the reduced electric field E/N and of the ionization rate and paves the way to full electric breakdown. In fact, already at time $t = 11.4 \mu\text{s}$, the minimum value of α_{eff} along the discharge axis is larger than 1060 m^{-1} which suffices to support a Townsend discharge according to (4.1).

The simulation can be continued until time $t = 35 \mu\text{s}$ when temperature reaches a maximum of about 20 000 K, but then our physical model with a majority of non-ionized air molecules is certainly no longer applicable.

We also carried out simulation (not included in this work) with $\eta = 0.3$, $\tau = 100 \text{ ns}$ and reduced initial seed size. We found the results to be qualitatively similar to the results obtained above. Since the VT relaxation timescale of 100 ns is much smaller as compared to $20 \mu\text{s}$, the heating takes place at a faster rate resulting in an earlier breakdown.

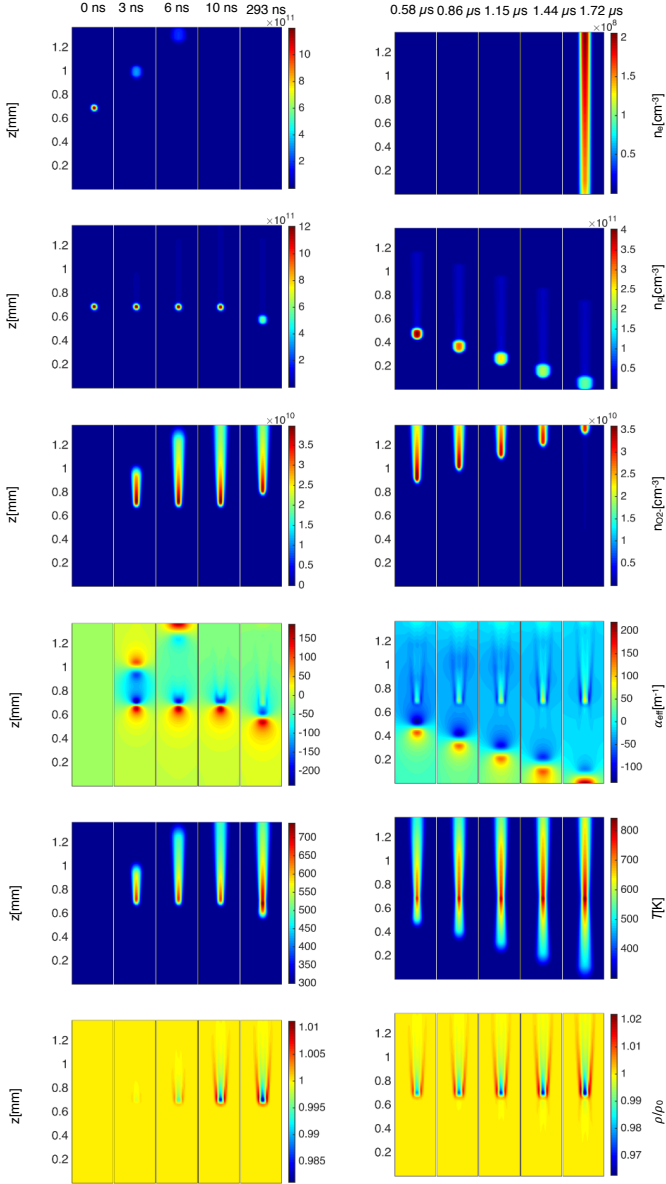


Figure 4.2: Evolution of electron number density n_e , positive ion number density n_p , negative ion number density $n_{O_2^-}$, effective Townsend coefficient α_{eff} , gas temperature T and normalized gas density ρ/ρ_0 . The initial seed of electrons and positive ions is placed on the discharge axis ($r = 0$) at $z = 0.69$ mm. The gas is air at 1 bar and a voltage of 3.7 kV is applied to a gap of 1.38 mm. The temporal sequence for $t = 0, 3, 6, 10$ and 293 ns in the left panel are plotted with one color scheme for densities and fields, and the sequence for $t = 580$ and 867 ns, and 1.15, 1.44, 1.72 μs in the right panel with another color scheme. The full height of the system is shown, but the plots are truncated in the radial direction.

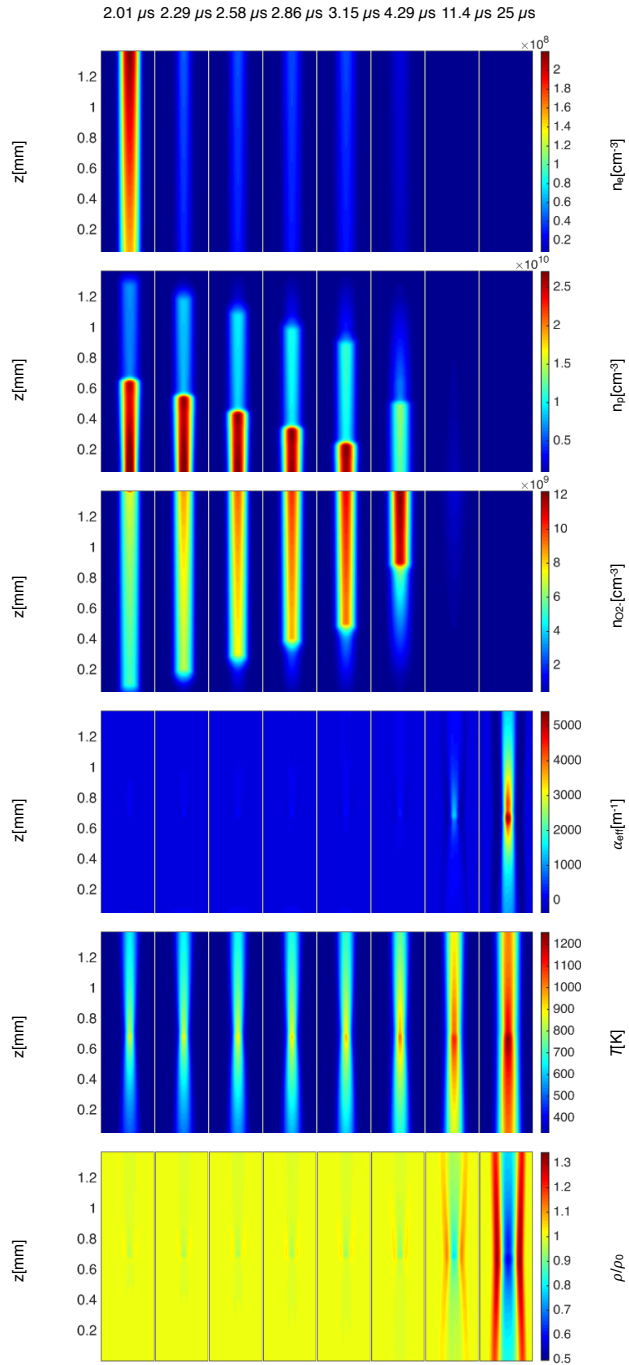


Figure 4.3: Continuation of the previous figure with plots for $t = 2.01, 2.29, 2.58, 2.86, 3.15, 4.29, 11.4$ and $25 \mu\text{s}$, again with a different color scheme for the densities and fields.

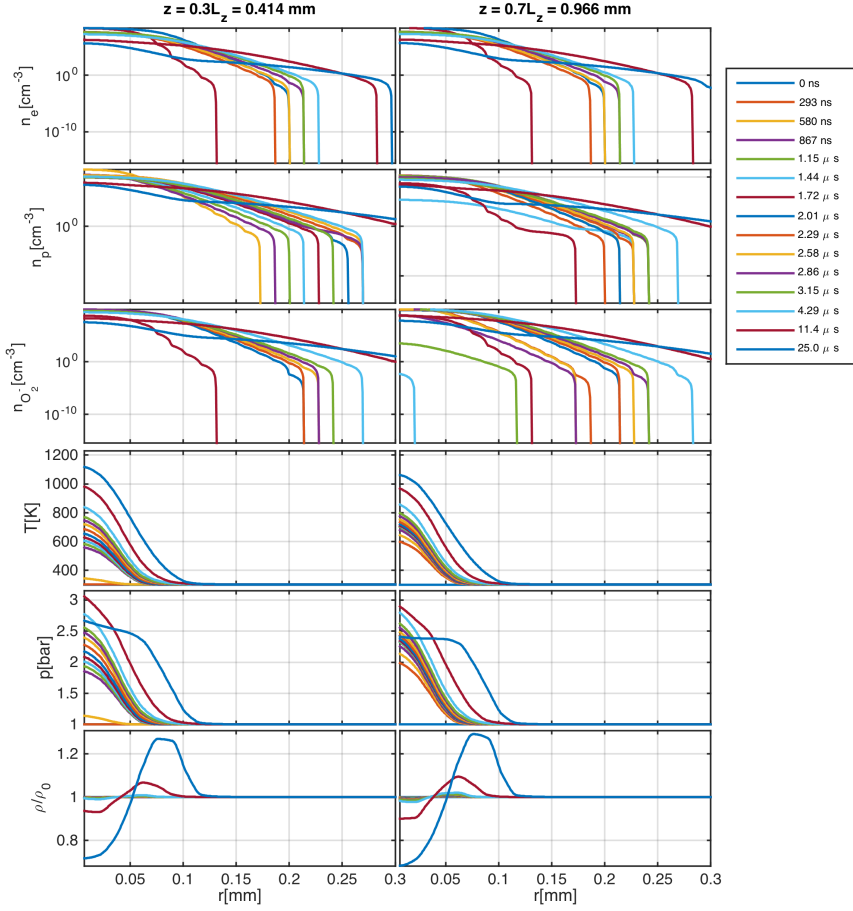


Figure 4.4: Temporal evolution for the charged particle densities, gas temperature, gas pressure and relative gas density at $z = 0.3L_z = 0.414$ mm and $z = 0.7L_z = 0.966$ mm. Plotted are time steps $t = 0 \mu\text{s}, 0.29 \mu\text{s}, 0.58 \mu\text{s}, 0.86 \mu\text{s}, 1.15 \mu\text{s}, 1.44 \mu\text{s}, 1.72 \mu\text{s}, 2.01 \mu\text{s}, 2.29 \mu\text{s}, 2.58 \mu\text{s}, 2.86 \mu\text{s}, 3.15 \mu\text{s}, 4.29 \mu\text{s}, 11.4 \mu\text{s}$ and $25 \mu\text{s}$.

4.5 Summary and Outlook

We have simulated the dynamics of a coupled system of electric discharge and background gas in air at standard temperature and pressure in a short gap in plane-to-plane electrode configuration, assuming cylindrical symmetry. Our discharge model includes electron impact ionization, attachment and secondary emission in fluid approximation with coefficients depending on electric field and gas density, and the hydrodynamic model for the carrier gas accounts for Ohmic heating and the associated gas expansion.

To treat the widely varying time scales of electron and ion dynamics, gas heating and expansion, we have derived a reduced model on the (slow) time scale of ion motion. In previous work [63], we had used the reduced model only. In the present paper, we show that this approach leads to missing some heat deposition during the initial stage, and to errors at well defined later stages. We therefore now switch between the full model on the (fast) electron timescale and the reduced model on the (slow) ion timescale. This adaptivity in time largely enhances computational efficiency.

Our simulations show how the air gap eventually breaks down due to gas heating, rather than due to the streamer mechanism which is driven by space charge effects. We observe a cyclic process: positive ions hit the cathode, liberate electrons via secondary emission, and these electrons feed the discharge channel by producing more electrons and ions via impact ionization. The newly created ions again drift toward the cathode. The moving electrons and ions heat the gas, the gas expands, and eventually electric breakdown occurs in an unchanged electric field due to the decreased gas density near the discharge axis.

While in the present work we switched by hand from the full to the reduced model, we will study the switching criteria in more detail in future work to provide automatic time adaptivity of the computational code. We also intend to include more chemical and ion species in future 2D modeling to better understand the combined contributions of gas expansion and changing gas composition.

4.6 Numerical Implementation

In this appendix we discuss the numerical methods we employed to discretize our equations. We recall that in this work we have used a strategy where we first carry out the simulation of the full model (drift-diffusion-reaction model for electric discharge) coupled to the Euler equations on the timescale of electron motion. After the primary electrons have left the system we switch to the reduced model for electric discharge coupled to the Euler equations and carry out the simulation on the timescale of ion motion. Below we briefly describe the discretization schemes we employed to carry out the simulation in both these situations.

We adopt a finite volume approach for computation whereby we employ a conservative flux limited scheme [68, 48] with Koren flux limiter for discretization

in space. These discretizations are similar to those by Montijn *et al.* [22]. The model after discretization in space is a differential algebraic system. Formally, the system can be written as

$$d_t P = F(P, Q), \quad (4.41)$$

$$0 = G(P, Q), \quad (4.42)$$

where in the full model (4.41) represents the system of coupled ODEs describing the electrons, ions and gas variables and (4.42) describes the electric field. In the reduced model (4.41) represents the system of coupled ODEs describing the ions and gas variables and (4.42) describes the electrons and the electric field. Now the equation (4.42) can be solved in terms of variable P such that

$$Q = H(P). \quad (4.43)$$

The details of actual implementation will be described below (App. A.1). The resulting system of ODEs then is given by

$$d_t P = \Psi(P), \text{ where } \Psi(P) = F(P, H(P)). \quad (4.44)$$

This is evolved in time using a second-order Runge-Kutta method (explicit trapezoidal rule) [49]. In terms of the original system (1.1), this can be described in two stages, the first of which reads

$$P_{n+1}^* = P_n + \Delta t F(P_n, Q_n), \quad (4.45)$$

$$Q_{n+1}^* = H(P_{n+1}^*), \quad (4.46)$$

where P_n and Q_n represent the value of the variables P and Q at time $t = t_n$. Finally, the value of the variables at time $t = t_{n+1}$ are

$$P_{n+1} = P_n + \frac{1}{2} \Delta t F(P_n, Q_n) + \frac{1}{2} \Delta t F(P_{n+1}^*, Q_{n+1}^*), \quad (4.47)$$

$$Q_{n+1} = H(P_{n+1}). \quad (4.48)$$

The time-step is chosen such that the CFL condition for numerical stability is satisfied.

4.6.1 Computation of electron density in reduced model

In the reduced model we compute the electron density that now is of the form (4.42), as follows. For simplicity, we first discuss the strategy in 1D case and later give the generalized form in 2D. The equation describing the electron dynamics

in the reduced model of electric discharge that we adopt (after comparison with the drift-diffusion-reaction model) is:

$$\frac{\partial}{\partial x} j_e = S_e, \quad (4.49)$$

where the total current density $j_e = -n_e \mu_e E$ and source term $S_e = \alpha |j_e|$. We have set electron diffusion coefficient D_e to zero in the total electron current density. For a given time t , the above equation is an ODE with x as the independent variable. The initial condition is given by $j_e^b = \gamma j_p^b$, where j_p^b is the ion current density evaluated at the cathode and γ denotes the secondary emission coefficient. We can then adopt an ODE method (with x serving as the independent variable) to compute the electron current density (and hence the electron number density $n_e = |j_e|/(\mu_e E)$) at the next step given the value at the previous step. Note that in the reduced model the contribution of electrons to the space charge is negligible and the electric field is completely determined by the distribution of the ions. For discretization we use the extrapolated second-order BDF2 method applied to (4.49) in backward direction:

$$\frac{3}{2} j_e^m - 2 j_e^{m+1} + \frac{1}{2} j_e^{m+2} = -2 \Delta x S_e^{m+1} + \Delta x S_e^{m+2}, \quad (4.50)$$

where Δx is the width of a grid cell and m is the position index such that $m = M - 2, M - 3, \dots, 3, 2, 1$, where M is the number of grid cells in 1D. This two-step method needs j_e^M and j_e^{M-1} as starting values. To compute j_e^M we use the Euler method,

$$j_e^M = j_e^b - \frac{\Delta x}{2} S_e^b, \quad (4.51)$$

where j_e^b and S_e^b denote the electron current density and the source term for electrons evaluated at the cathode respectively. Furthermore, j_e^{M-1} is computed by integrating eq. (4.49) using a second-order Runge Kutta method (explicit trapezoidal rule) with j_e^M as initial value and time-step equal to Δx as in App. A.1

The strategy described above can be generalized to 2D-cylindrically symmetric geometry. The equation describing the electron dynamics is:

$$\frac{\partial}{\partial z} j_{ez} + \frac{1}{r} \frac{\partial}{\partial r} j_{er} = S_e, \quad (4.52)$$

where $j_{ez} = -n_e \mu_e E_z$, $j_{er} = -n_e \mu_e E_r$ and $S_e = \alpha \mu_e |\mathbf{E}| n_e$. The above equation can be written as:

$$\frac{\partial}{\partial z} j_{ez} = \bar{S}_e, \quad (4.53)$$

where \bar{S}_e is the modified source term given by:

$$\bar{S}_e = S_e - \frac{1}{r} \frac{\partial}{\partial r} j_{er}. \quad (4.54)$$

The eq.(4.53) can now be integrated in exactly the same way as in the 1D-case with z serving as the independent variable.

4.6.2 Implementation of heating term in Euler system

The source term describing Joule heating of the gas is according to equation (4.20)

$$S_{\xi}(\mathbf{r}, t) = \eta P(\mathbf{r}, t) + (1 - \eta) \int_{-\infty}^t P(\mathbf{r}, t') e^{-(t-t')/\tau} \frac{dt'}{\tau}, \quad (4.55)$$

where τ denotes the relaxation time constant of the excited vibrational energy states of the gas. The calculation of the temporal integral can be simplified by noting that

$$\begin{aligned} \mathcal{I}(\mathbf{r}, t + \Delta t) &:= \int_{-\infty}^{t+\Delta t} P(\mathbf{r}, t') e^{-(t+\Delta t-t')/\tau} \frac{dt'}{\tau} \\ &= e^{-\Delta t/\tau} \mathcal{I}(\mathbf{r}, t) + \int_t^{t+\Delta t} P(\mathbf{r}, t') e^{(t+\Delta t-t')/\tau} \frac{dt'}{\tau}, \end{aligned} \quad (4.56)$$

so we only have to perform the integral from time t to $t + \Delta t$ to update the integral \mathcal{I} . The source term can be computed to desired accuracy by computing the integral terms via quadrature rules; we have used the simple Trapezoidal rule.

4.6.3 Implementation of outflow boundary condition in the Euler system

To implement the outflow boundary condition in the Euler system on the outer radial boundary ($r = L_r$) we extrapolate ρ , v_r and p . For that we fit a second-order polynomial for the variables ρ , v_r and p through the points (r_{M-2}, z_n) , (r_{M-1}, z_n) and (r_M, z_n) , where the index M refers to the outermost cell-centers in the radial direction and n refers to index in the z -direction. Thereafter, we compute the value of the variable (ρ , v_r and p) by evaluating the respective polynomial on the outer radial boundary.

Chapter 5

Adaptive selection of sampling points for uncertainty quantification

We present a simple and robust strategy for the selection of sampling points in Uncertainty Quantification. The goal is to achieve the fastest possible convergence in the cumulative distribution function of a stochastic output of interest. We assume that the output of interest is the outcome of a computationally expensive nonlinear mapping of an input random variable, whose probability density function is known. We use a radial function basis to construct an accurate interpolant of the mapping. This strategy enables adding new sampling points one at a time, *adaptively*. This takes into full account the previous evaluations of the target nonlinear function. We present comparisons with a stochastic collocation method based on the Clenshaw-Curtis quadrature rule, and with an adaptive method based on hierarchical surplus, showing that the new method often results in a large computational saving.

1

¹This chapter is based on "Adaptive selection of sampling points for Uncertainty Quantification." by E. Camporeale, A. Agnihotri and C. Rutjes. *International Journal for Uncertainty Quantification* 7, no. 4 (2017).

5.1 Introduction

We address one of the fundamental problems in Uncertainty Quantification (UQ): the mapping of the probability distribution of a random variable through a non-linear function. Let us assume that we are concerned with a specific physical or engineering model which is computationally expensive. The model is defined by the map $g : \mathbb{R} \rightarrow \mathbb{R}$. It takes a parameter X as input, and produces an output Y , $Y = g(X)$. In this paper we restrict ourselves to a proof-of-principle one-dimensional case. Let us assume that X is a random variable distributed with probability density function (pdf) P_X . The Uncertainty Quantification problem is the estimation of the pdf P_Y of the output variable Y , given P_X . Formally, the problem can be simply cast as a coordinate transformation and one easily obtains

$$P_Y(y) = \sum_{x \in \{x|g(x)=y\}} \frac{P_X(x)}{|\det J(x)|}, \quad (5.1)$$

where $J(x)$ is the Jacobian of $g(x)$. The sum over all x such that $g(x) = y$ takes in account the possibility that g may not be injective. If the function g is known exactly and invertible, Eq.(5.1) can be used straightforwardly to construct the pdf $P_Y(y)$, but this is of course not the case when the mapping g is computed via numerical simulations.

Several techniques have been studied in the last couple of decades to tackle this problem. Generally, the techniques can be divided in two categories: intrusive and non-intrusive [69, 70, 71]. Intrusive methods modify the original, *deterministic*, set of equations to account for the stochastic nature of the input (random) variables, hence eventually dealing with stochastic differential equations, and employing specific numerical techniques to solve them. Classical examples of intrusive methods are represented by Polynomial Chaos expansion [72, 73, 74, 75], and stochastic Galerkin methods [76, 77, 78, 79].

On the other hand, the philosophy behind non-intrusive methods is to make use of the deterministic version of the model (and the computer code that solves it) as a black-box, which returns one deterministic output for any given input. An arbitrary large number of solutions, obtained by sampling the input parameter space, can then be collected and analyzed in order to reconstruct the pdf $P_Y(y)$.

The paradigm of non-intrusive methods is perhaps best represented by Monte Carlo (MC) methods [80, 81]: one can construct an ensemble of input parameters $\{X_n | n = 1, \dots, N\}$ (N typically large) distributed according to the pdf $P_X(x)$, run the corresponding ensemble of simulations $g : X \rightarrow Y$, and process the outputs $\{Y_n | n = 1, \dots, N\}$. MC methods are probably the most robust of all the non-intrusive methods. Their main shortcoming is the slow convergence of the method, with a typical convergence rate proportional to \sqrt{N} . For many applications quasi-Monte Carlo (QMC) methods [80, 82] are now preferred to MC methods, for their faster convergence rate. In QMC the pseudo-random

generator of samples is replaced by more uniform distributions, obtained through so-called quasi-random generators [83, 84].

It is often said that MC and QMC do not suffer the ‘curse of dimensionality’ [85, 86, 87], in the sense that the convergence rate (but not the actual error!) is not affected by the dimension D of the input parameter space. Therefore, they represent the standard choice for large dimensional problems. On the other hand, when the dimension D is not very large, collocation methods [88, 89, 90] are usually more efficient.

Yet a different method that focuses on deriving a deterministic differential equation for cumulative distribution functions has been presented, e.g., in [91, 92]. This method is however not completely black-box.

Collocation methods recast an UQ problem as an interpolation problem. In collocation methods, the function $g(x)$ is sampled in a small (compared to the MC approach) number of points (‘collocation points’), and an interpolant is constructed to obtain an approximation of g over the whole input parameter space, from which the pdf $P_Y(y)$ can be estimated.

The question then arises on how to effectively choose the collocation points. Recalling that every evaluation of the function g amounts to performing an expensive simulation, the challenge resides in obtaining an accurate approximation of P_Y with the least number of collocation points. Indeed, a very active area of research is represented by collocation methods that use sparse grids, so to avoid the computation of a full-rank tensorial product, particularly for model order reduction (see, e.g., [93, 94, 95, 96, 97, 98, 99])

As the name suggests, collocation methods are usually derived from classical quadrature rules [100, 101, 102].

The type of pdf P_X can guide the choice of the optimal quadrature rule to be used (i.e., Gauss-Hermite for a Gaussian probability, Gauss-Legendre for a uniform probability, etc. [88]). Furthermore, because quadratures are associated with polynomial interpolation, it becomes natural to define a global interpolant in terms of a Lagrange polynomial [103]. Also, choosing the collocation points as the abscissas of a given quadrature rule makes sense particularly if one is only interested in the evaluation of the statistical moments of the pdf (i.e., mean, variance, etc.) [104].

On the other hand, there are several applications where one is interested in the approximation of the full pdf P_Y . For instance, when g is narrowly peaked around two or more distinct values, its mean does not have any statistical meaning. In such cases one can wonder whether a standard collocation method based on quadrature rules still represents the optimal choice, in the sense of the computational cost to obtain a given accuracy.

From this perspective, a downside of collocation methods is that the collocation points are chosen a priori, without making use of the knowledge of $g(x)$ acquired at previous interpolation levels. For instance, the Clenshaw-Curtis (CC) method uses a set of points that contains ‘nested’ subset, in order to re-use all

the previous computations, when the number of collocation points is increased. However, since the abscissas are unevenly spaced and concentrated towards the edge of the domain (this is typical of all quadrature rules, in order to overcome the Runge phenomenon [103, 105]), it is likely that the majority of the performed simulations will not contribute significantly in achieving a better approximation of P_Y . Stated differently, one would like to employ a method where each new sampling point is chosen in such a way to result in the fastest convergence rate for the approximated P_Y , in contrast to a set of points defined a priori.

As a matter of fact, because the function g is unknown, a certain number of simulations will always be redundant, in the sense that they will contribute very little to the convergence of P_Y . The rationale for this work is to devise a method to minimize such a redundancy in the choice of sampling points while achieving fastest possible convergence of P_Y .

Clearly, this suggests to devise a strategy that chooses collocation points *adaptively*, making use of the knowledge of the interpolant of $g(x)$, which becomes more and more accurate as more points are added.

A well known adaptive sampling algorithm is based on the calculation of the so-called hierarchical surplus [96, 106, 98, 107, see e.g.]. This is defined as the difference, between two levels of refinement, in the solution obtained by the interpolant. Although this algorithm is quite robust, and it is especially efficient in detecting discontinuities, it has the obvious drawback that it can be prematurely terminated, whenever the interpolant happens to exactly pass through the true solution on a point where the hierarchical surplus is calculated, no matter how inaccurate the interpolant is in close-by regions (see Figure 5.1 for an example).

The goal of this paper is to describe an alternative strategy for the adaptive selection of sampling points. The objective in devising such strategy is to have a simple and robust set of rules for choosing the next sampling point. The paper is concerned with a proof-of-principle demonstration of our new strategy, and we will focus here on one dimensional cases and on the case of uniform P_X only, postponing the generalization to multiple dimensions to future work. It is important to appreciate that the stated goal of this work is different from the traditional approach followed in the overwhelming majority of works that have presented sampling methods for UQ in the literature. Indeed, it is standard to focus on the convergence of the nonlinear unknown function $g(x)$, trying to minimize the interpolation error on $g(x)$, for a given number of sampling points. On the other hand, we will show that the convergence rates of $g(x)$ and of its cumulative distribution function can be quite different. Our new strategy is designed to achieve the fastest convergence on the latter quantity, which is ultimately the observable quantity of an experiment.

The paper is organized as follows. In Section 2 we define the mathematical methods used for the construction of the interpolant and show our adaptive strategy to choose a new collocation points. In Section 3 we present some numerical

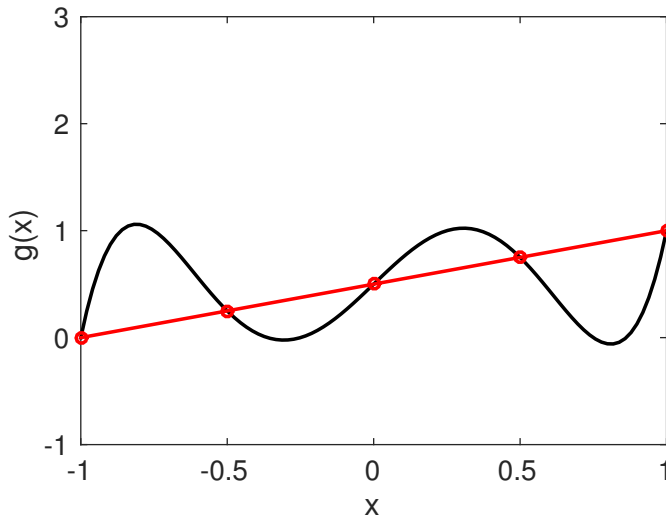


Figure 5.1: Example for which the algorithm based on hierarchical surplus fails. The function $g(x) = \frac{256}{30}x^5 - \frac{32}{3}x^3 + \frac{79}{30}x + \frac{1}{2}$ (in black) goes exactly through the red straight line at the points $x = -1, -0.5, 0, 0.5, 1$. Calculating the piecewise linear interpolant between two ($x = -1, 1$), three ($x = -1, 0, 1$), and five ($x = -1, -\frac{1}{2}, 0, \frac{1}{2}, 1$) points would result in a null hierarchical surplus on these points.

examples and comparisons with the Clenshaw-Curtis collocation method, and the adaptive method based on hierarchical surplus. Finally, we draw our conclusions in Section 4.

5.2 Mathematical methods

5.2.1 Clenshaw-Curtis (CC) quadrature rule

In Section 3, we compare our method with the CC method, which is the standard appropriate collocation method for a uniform P_X . Here, we recall the basic properties of CC, for completeness. The Clenshaw-Curtis (CC) quadrature rule uses the extrema of a Chebyshev polynomial (the so-called ‘extrema plus endpoints’ collocation points in [108]) as abscissas. They are particularly appealing to be used as collocation points in UQ, because a certain subset of them are nested. Specifically, they are defined, in the interval $[-1, 1]$ as:

$$x_i = -\cos\left(\frac{\pi(i-1)}{N-1}\right) \quad i = 1, \dots, N. \quad (5.2)$$

One can notice that the the set of $N = 2^w + 1$ points is fully contained in the set of $N = 2^{w+1} + 1$ points (with w an arbitrary integer, referred to as the level

of the set). In practice this means that one can construct a nested sequence of collocation points with $N = 3, 5, 9, 17, 33, 65, 129, \dots$, re-using all the previous evaluations of g .

Collocation points based on quadratures are optimal to calculate moments ²:

$$\mu_Y^p = \int y^p P_Y(y) dy = \int g(x)^p P_X(x) dx, \quad (5.3)$$

where we used the identity relation,

$$P_Y(y) dy = P_X(x) dx. \quad (5.4)$$

It is known that integration by quadrature is very accurate (for smooth enough integrand), and the moments can be readily evaluated, without the need to construct an interpolant:

$$\mu_Y^p \simeq \sum_i w_i (g(x_i))^p, \quad (5.5)$$

where the weights w_i can be computed with standard techniques (see, e.g. [104]). The interpolant for the CC method is the Lagrange polynomial.

5.2.2 Selection of collocation points based on hierarchical surplus

The hierarchical surplus algorithm is widely used for interpolation on sparse grids. It is generally defined as the difference between the value of an interpolant at the current and previous interpolation levels [96]:

$$\Delta^n = \tilde{g}^n - \tilde{g}^{n-1} \quad (5.6)$$

The simplest algorithm prescribes a certain tolerance and looks for all the point at the new level where the hierarchical surplus is larger than the tolerance. The new sampling points (at the next level, $n + 1$) will be the neighbors (defined with a certain rule) of the points where this condition is met. In one-dimension, the algorithm is extremely simple because the neighbors are defined by only two points, that one can define in such a way that cells are always halved. In this work, we compare our new method with a slightly improved version of the hierarchical surplus algorithm. The reason is because we do not want our comparisons to be dependent on the choice of an arbitrary tolerance level, and we want to be able to add new points two at the time. Hence, we define a new interpolation level by adding only the two neighbors of the point with the largest hierarchical surplus. All the previous hierarchical

²Here p on the left-hand side is a label, such that μ^1 is the mean, μ^2 is the variance, and so on. On the right-hand side it is an exponent.

surpluses that have been calculated, but for which new points have not been added yet are kept. The pseudo-code of the algorithm follows. The interpolant is understood to be piece-wise linear interpolation, and the grid is $x \in [-1, 1]$.

Algorithm 1: Hierarchical surplus algorithm

- 1 Calculate the interpolant on the grid $x = \{-1, 0, 1\}$.
 - 2 Define $x_h = \{-1/2, 1/2\}$ and add them on the grid
 - 3 **while** *Not converged* **do**
 - 4 Calculate the interpolant on the new grid
 - 5 Calculate the hierarchical surplus on the last two entries of x_h and
store them in the vector h_s
 - 6 Find the largest hierarchical surplus in h_s , remove it from h_s and
remove the corresponding x from x_h
 - 7 Append the two neighbors to x_h and add them to the grid
 - 8 **end**
-

5.2.3 Multiquadric biharmonic radial basis

We use a multiquadric biharmonic radial basis function (RBF) with respect to a set of points $\{x_i\}$, with $i = 1, \dots, N$, defined as:

$$\Phi_i(x, c) = \sqrt{(x - x_i)^2 + c_i^2}, \quad (5.7)$$

where c_i are free parameters (referred to as shape parameters). The function $g(x)$ is approximated by the interpolant $\tilde{g}(x)$ defined as

$$\tilde{g}(x) = \sum_{i=1}^N \lambda_i \Phi_i(x, c). \quad (5.8)$$

The weights λ_i are obtained by imposing that $g(x_i) = \tilde{g}(x_i)$ for each sampling point in the set, namely the interpolation error is null at the sampling points. This results in solving a linear system for $\lambda = (\lambda_1, \dots, \lambda_N)$ of the form $A\lambda^T = g(\mathbf{x})^T$, with A a real symmetric $N \times N$ matrix. We note that, by construction, the linear system will become more and more ill-conditioned with increasing N , for fixed values of c . This can be easily understood because when two points become closer and closer the corresponding two rows in the matrix A become less and less linearly independent. To overcome this problem one needs to decrease the corresponding values of c . In turns, this means that the interpolant $\tilde{g}(x)$ will tend to a piece-wise linear interpolant for increasingly large N .

5.2.4 New adaptive selection of collocation points

We focus, as the main diagnostic of our method, on the cumulative distribution function (cdf) $C(y)$, which is defined as

$$C(y) = \int_{y_{\min}}^y P_Y(y) dy, \quad (5.9)$$

where $y_{\min} = \min g(x)$. As it is well known, the interpretation of the cumulative distribution function is that, for a given value y^* , $C(y^*)$ is the probability that $g(x) \leq y^*$. Of course, the cdf $C(y)$ contains all the statistical information needed to calculate any moment of the distribution, and can return the probability density function $P_Y(y)$, upon differentiation. Moreover, the cdf is always well defined between 0 and 1. The following two straightforward considerations will guide the design of our *adaptive selection strategy*. A first crucial point, already evident from Eq. (5.1), is whether or not $g(x)$ is bijective. When $g(x)$ is bijective this translates to the cdf $C(y)$ being continuous, while a non-bijective function $g(x)$ produces a cdf $C(y)$ which is discontinuous. It follows that intervals in x where $g(x)$ is constant (or nearly constant) will map into a single value $y = g(x)$ (or a very small interval in y) where the cdf will be discontinuous (or ‘nearly’ discontinuous). Secondly, an interval in x with a large first derivative of $g(x)$ will produce a nearly flat cdf $C(y)$. This is again clear by noticing that the Jacobian J in Eq. (5.1) ($dg(x)/dx$ in one dimension) is in the denominator, and therefore the corresponding $P_Y(y)$ will be very small, resulting in a flat cdf $C(y)$.

Loosely speaking one can then state that regions where $g(x)$ is flat will produce large jumps in the cdf $C(y)$ and, conversely, regions where the $g(x)$ has large jumps will map in to a nearly flat cdf $C(y)$. From this simple considerations one can appreciate how important it is to have an interpolant that accurately capture both regions with *very large* and *very small* first derivative of $g(x)$. Moreover, since the cdf $C(y)$ is an integrated quantity, interpolation errors committed around a given y will propagate in the cdf for all larger y values. For this reason, it is important to achieve a global convergence with interpolation errors that are of the same order of magnitude along the whole domain.

The adaptive section algorithm works as follows. We work in the interval $x \in [-1, 1]$ (every other interval where the support of $g(x)$ is defined can be rescaled to this interval). We denote with $\{x_i\}$ the sampling set which we assume is always sorted, such that $x_i < x_{i+1}$. We start with 3 points: $x_1 = -1$, $x_2 = 0$, $x_3 = 1$. For the robustness and the simplicity of the implementation we choose to select a new sampling point always at equal distance between two existing points. One can decide to limit the ratio between the largest and smallest distance between adjacent points: $r = \max\{d_i\} / \min\{d_i\}$ (with $i = 1, \dots, N - 1$), where d_i is the distance between the points x_{i+1} and x_i . This avoids to keep refining small intervals when large intervals might still be under-resolved, thus aiming for the above mentioned global convergence over the whole support. At each iteration

we create a list of possible new points, by halving every interval, excluding the points that would increase the value of r above the maximum desired (note that r will always be a power of 2). We calculate the first derivative of $\tilde{g}(x)$ at these points, and alternatively choose the point with largest/smallest derivative as the next sampling point. Notice that, by the definition of the interpolant, Eq. (5.8), its first derivative can be calculated exactly as:

$$\frac{d\tilde{g}(x)}{dx} = \sum_{i=1}^N \lambda_i \frac{d\Phi_i(x, c)}{dx} \quad (5.10)$$

without having to recompute the weights λ_i . At each iteration the shape parameters c_i are defined at each points, as $c_i = 0.85 \cdot \min(d_{i-1}, d_i)$, i.e. they are linearly rescaled with the smallest distance between the point x_i and its neighbors. The pseudo-code of the algorithm follows.

Algorithm 2: Adaptive selection of sampling points

```

9 while Not converged do
10    $x_{\text{guess}} \leftarrow 0.5 \cdot (x_i + x_{i+1})$ 
11   Exclude points in  $x_{\text{guess}}$  such that  $r = \max\{d_i\} / \min\{d_i\} > R$ 
12   Calculate  $\tilde{g}^n(x)'$  through (5.10) at  $\{x_{\text{guess}}\}$ 
13   Alternatively choose  $x_{\text{guess}}$  with largest/smallest values of  $|\tilde{g}^n(x)'|$  as
       new collocation point
14   Calculate new weights  $\lambda_i$ 

```

5.3 Numerical examples

In this section we present and discuss four numerical examples where we apply our adaptive selection strategy. In this work we focus on a single input parameter and the case of constant probability $P_X = 1/2$ in the interval $x \in [-1, 1]$, and we compare our results against the Clenshaw-Curtis, and the hierarchical surplus methods. We denote with $\tilde{g}^n(x)$ the interpolant obtained with a set of n points (hence the iterative procedure starts with $\tilde{g}^3(x)$). A possible way to construct the cdf $C(y)$ from a given interpolant $\tilde{g}^n(x)$ would be to generate a sample of points in the domain $[-1, 1]$, randomly distributed according to the pdf $P_X(x)$, collecting the corresponding values calculated through Eq. (5.8), and constructing their cdf. Because here we work with a constant $P_X(x)$, it is more efficient to simply define a uniform grid in the domain $[-1, 1]$ where to compute $\tilde{g}^n(x)$. In the following we will use, in the evaluation of the cdf $C(y)$, a grid in y with $N_y = 10001$ points equally spaced in the interval $[\min \tilde{g}^n(x), \max \tilde{g}^n(x)]$, and a grid in x with $N_x = 1001$ points equally spaced in the interval $[-1, 1]$. We define the following

errors:

$$\varepsilon_C = \frac{\|C(\tilde{g}^n(x)) - C(g(x))\|_2}{\sqrt{N_y}} \quad (5.11)$$

$$\varepsilon_g = \frac{\|\tilde{g}^n(x) - g(x)\|_2}{\sqrt{N_x}} \quad (5.12)$$

where $\|\cdot\|_2$ denotes the L_2 norm. It is important to realize that the accuracy of the numerically evaluated cdf $C(y)$ will always depend on the binning of y , i.e. the points at which the cdf is evaluated. As we will see in the following examples, the error ε_C saturates for large N , which thus is an artifact of the finite bin size. We emphasize that, differently from most of the previous literature, our strategy focuses on converging rapidly in ε_C , rather than in ε_g . Of course, a more accurate interpolant will always result in a more accurate cdf, however the relationship between a reduction in ε_g and a corresponding reduction in ε_C is not at all trivial. This is because the relation between $P_X(x)$ and $P_Y(y)$ is mediated by the Jacobian of $g(x)$, and it also involves the bijectivity of g .

Finally, we study the convergence of the mean μ_Y , see equation 5.3, and the variance σ_Y^2 , which is defined as

$$\sigma_Y^2 = \int_{-1}^1 (\tilde{g}(x) - \mu_Y)^2 P_X(x) dx. \quad (5.13)$$

These will be calculated by quadrature for the CC methods, and with an integration via trapezoidal method for the adaptive methods.

We study two analytical test cases:

- Case 1: $g(x) = \arctan(10^3 x^3)$;
- Case 2: $g(x) = \frac{1}{(2 + \sin(3\pi x))^2}$;

and two test cases where an analytical solution is not available, and the reference $g(x)$ will be calculated as an accurate numerical solution of a set of ordinary differential equations:

- Case 3: Lotka-Volterra model (predator-prey);
- Case 4: Van der Pol oscillator.

While Case 1 and 2 are more favorable to the CC method, because the functions are smooth and analytical, hence a polynomial interpolation is expected to produce accurate results, the latter two cases mimic applications of real interest, where the model does not produce analytical results, although $g(x)$ might still be smooth (at least piece-wise, in Case 4).

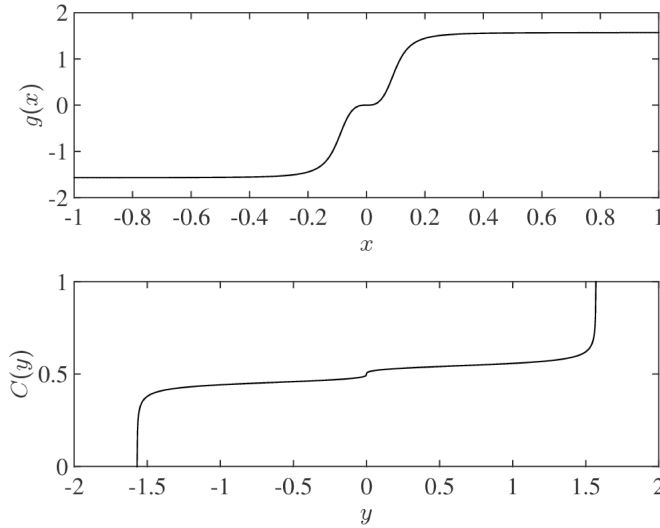


Figure 5.2: Case 1: $g(x) = \arctan(10^3 x^3)$. Top panel: $g(x)$; bottom panel: cdf $C(y)$.

5.3.1 Case 1: $g(x) = \arctan(10^3 x^3)$

In this case $g(x)$ is a bijective function, with one point ($x = 0$) where the first derivative vanishes. Figure 5.2 shows the function $g(x)$ (top panel) and the corresponding cdf $C(y)$ (bottom panel), which in this case can be derived analytically. Hence, we use the analytical expression of cdf $C(y)$ to evaluate the error ε_C . The convergence of ε_C and ε_g is shown in Figure 5.3 (top and bottom panels, respectively). Here and in all the following figures blue squares denote the new adaptive selection method, red dots are for the CC methods, and black line is for the hierarchical surplus method. We have run the CC method only for $N = 3, 5, 9, 17, 33, 65, 129$ (i.e. the points at which the collocation points are nested), but for a better graphical visualization the red dots are connected with straight lines. One can notice that the error for the new adaptive method is consistently smaller than for the CC method. From the top panel, one can appreciate the saving in computer power that can be achieved with our new method. Although the difference with CC is not very large until $N = 17$, at $N = 33$ there is an order of magnitude difference between the two. It effectively means that in order to achieve the same error $\varepsilon_C \sim 10^{-5}$, the CC method would run at least twice the number of simulations. The importance of focusing on the convergence of the cdf, rather than on the interpolant, is clear in comparing our method with the hierarchical surplus method. For instance, for $N = 80$, the two methods have a comparable error ε_g , but our method has achieved almost an order of magnitude more accurate solution in $C(y)$. Effectively, this means that

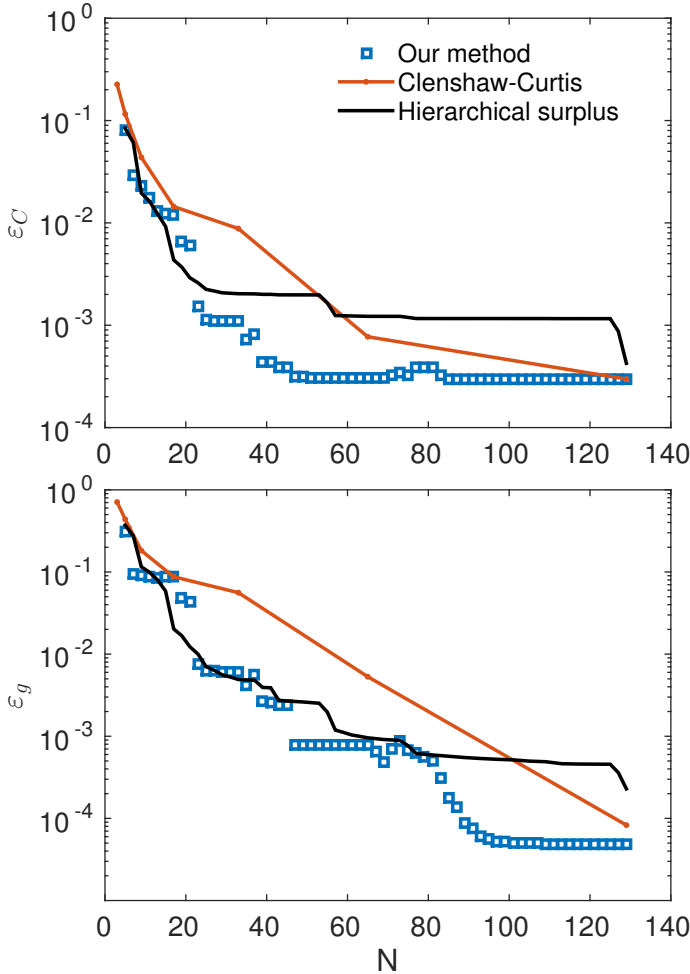


Figure 5.3: Case 1. Error ε_C (top) ε_g (bottom) as function of number of sampling points N . Blue squares: new adaptive selection method. Red dots: Clenshaw-Curtis. Black curve: adaptive method based on hierarchical surplus.

our method has sampled the new points less redundantly. In this case $g(x)$ is an anti-symmetric function with zero mean. Hence, any method that chooses sampling points symmetrically distributed around zero would produce the correct first moment μ_Y . We show in figure 5.4 the convergence of σ_Y^2 , as the absolute value of the different with the exact value σ_{an} , in logarithmic scale. Blue, red, and black lines represent the new adaptive method, the CC, and the hierarchical surplus methods, respectively (where again for the CC, simulations are only performed where the red dots are shown). The exact value is $\sigma_{an}^2 = 2.102$. As

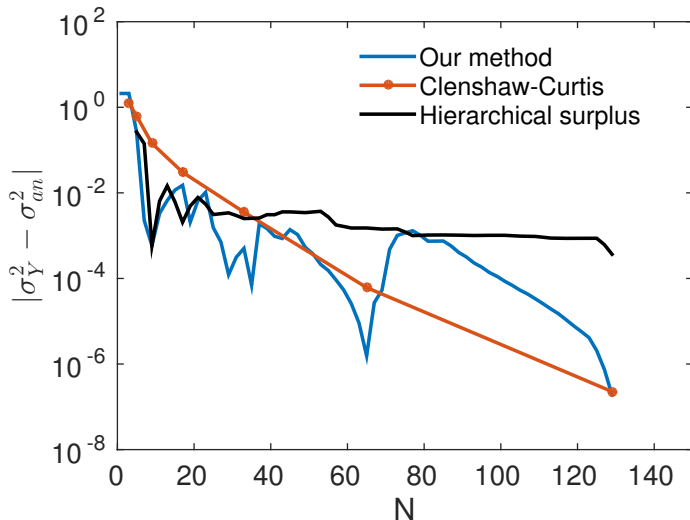


Figure 5.4: Case 1. Absolute error in the variance σ_Y^2 versus number of sampling points N . Blue: new adaptive selection method. Red: Clenshaw-Curtis. Black: adaptive method based on hierarchical surplus.

we mentioned, the CC method is optimal to calculate moments, since it uses quadrature. Although in our method the error does not decrease monotonically, it is comparable with the result for CC.

5.3.2 Case 2: $g(x) = \frac{1}{(2+\sin(3\pi x))^2}$

In this case the function $g(x)$ is periodic, and it presents, in the domain $x \in [-1, 1]$ three local minima ($y = 1/9$) and three local maxima ($y = 1$). The function and the cdf $C(y)$ are shown in Figure 5.5 (top and bottom panel, respectively). Figure 5.6 shows the error for this case (from now on the same format of Figure 5.3 will be used). The first consideration is that the hierarchical surplus method is the less accurate of the three. Second, ε_g is essentially the same for the CC and the new method, up to $N = 65$. For $N = 129$ the CC methods achieve a much accurate solution as compared to the new adaptive method, whose error has a much slower convergence. However, looking at the error in the cdf in top panel of Figure 5.6, the two methods are essentially equivalent. This example demonstrates that, in an UQ framework, the primary goal in constructing a good interpolant should not be to minimize the error of the interpolant with respect to the 'true' $g(x)$, but rather to achieve the fastest possible convergence on the cdf C_Y . Although, the two effects are intuitively correlated, they are not into a linear relationship. In other words, not all sample points in x count equally in minimizing ε_C . The convergence of μ_Y (exact value $\mu_{an} = 0.385$) and σ_Y^2 (exact

value $\sigma_{an} = 0.087$) is shown in Figures 5.7 and 5.8, respectively. It is interesting to notice that our method presents errors that are always smaller than the CC method, although the errors degrade considerably in the regions between two CC points, where the two adaptive methods yield comparable results.

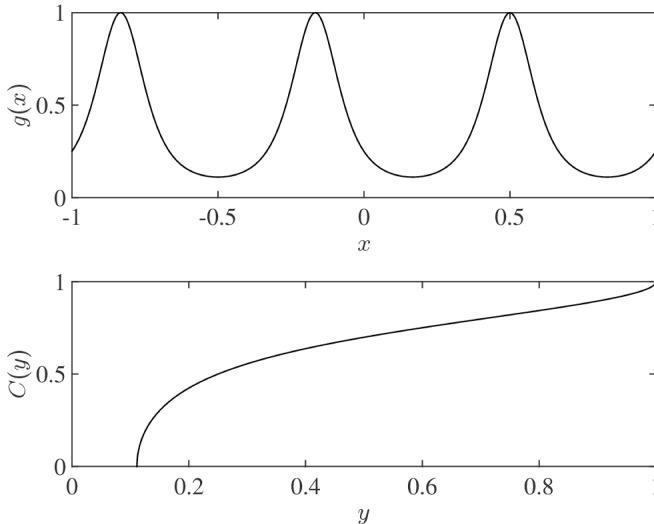


Figure 5.5: Case 2: $g(x) = \frac{1}{(2+\sin(3\pi x))^2}$. Top panel: $g(x)$; bottom panel: $C(y)$.

5.3.3 Case 3: Lotka-Volterra model (predator-prey)

The Lotka-Volterra model [109, 110, 111] is a well-studied model that exemplifies the interaction between two populations (predators and preys). This case is more realistic than Cases 1 and 2, as the solution of the model cannot be written in analytical form. As such, both the $g(x)$ and the cdf $C(y)$ used to compute the errors are calculated numerically. We use the following simple model:

$$\frac{dh(t)}{dt} = h(t) - (5x + 6)h(t)l(t) \quad (5.14)$$

$$\frac{dl(t)}{dt} = h(t)l(t) - l(t) \quad (5.15)$$

where $h(t)$ and $l(t)$ denote the population size for each species (say, horses and lions) as function of time. The ODE is easily solved in MATLAB, with the `ode45` routine, with an absolute tolerance set equal to 10^{-8} . We use, as initial conditions, $h(t=0) = l(t=0) = 1$, and we solve the equations for $t \in [0, 10]$. Clearly, the solution of the model depends on the input parameter x . We define our test function $g(x)$ to be the result of the model for the l population at time

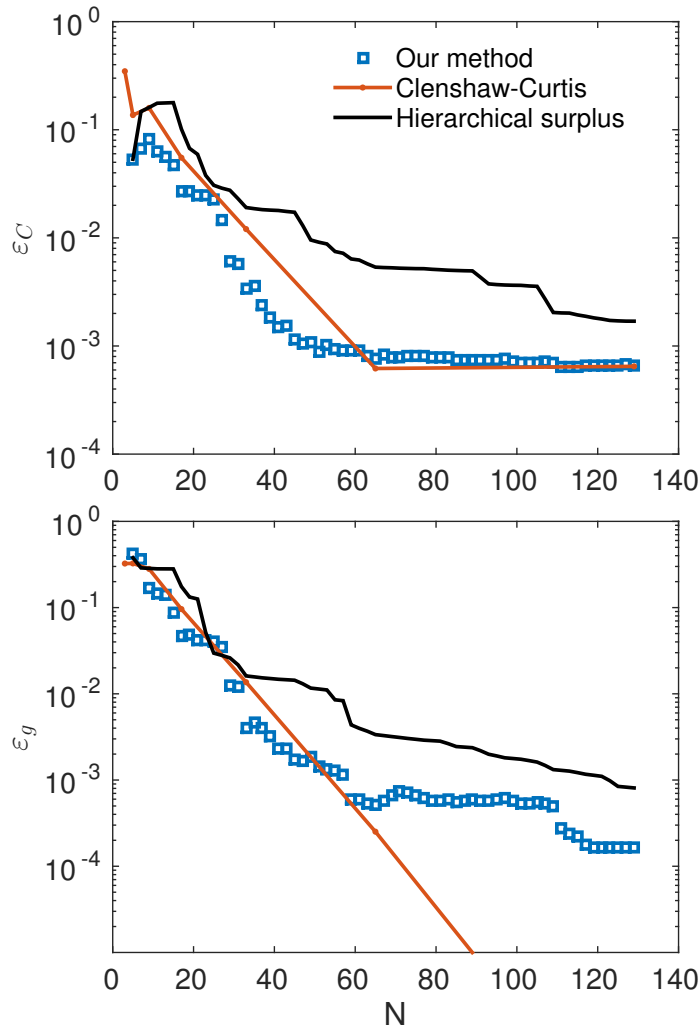


Figure 5.6: Case 2. Error ε_C (top) ε_g (bottom) as function of number of sampling points N . Blue squares: new adaptive selection method. Red dots: Clenshaw-Curtis. Black curve: adaptive method based on hierarchical surplus.

$t = 10$:

$$g(x) = l(t = 10, x). \tag{5.16}$$

The resulting function $g(x)$, and the computed cdf $C(y)$ are shown in Figure 5.9 (top and bottom panel, respectively). We note that, although $g(x)$ cannot be expressed as an analytical function, it is still smooth, and hence it does not present particular difficulties in being approximated through a polynomial interpolant.

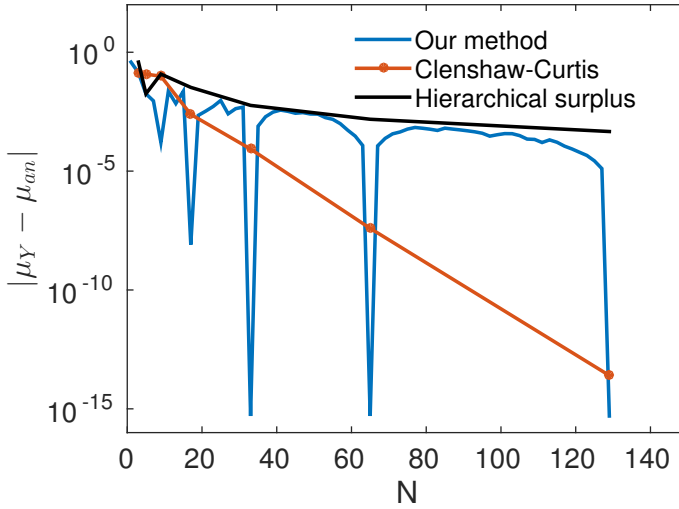


Figure 5.7: Case 2. Absolute error in the mean μ_Y versus number of sampling points N . Blue: new adaptive selection method. Red: Clenshaw-Curtis. Black: adaptive method based on hierarchical surplus.

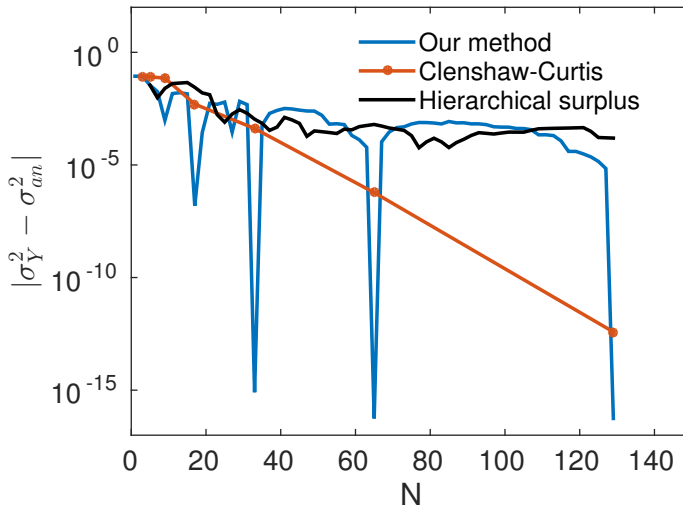


Figure 5.8: Case 2. Absolute error in the variance σ_Y^2 versus number of sampling points N . Blue: new adaptive selection method. Red: Clenshaw-Curtis. Black: adaptive method based on hierarchical surplus.

Indeed the error ε_g undergoes a fast convergence both for the adaptive methods and for the CC method (Figure 5.10). Once again, the new adaptive method is

much more powerful than the CC method in achieving a better convergence rate, and thus saving computational power, while the hierarchical surplus method is the worst of the three. Convergence of μ_Y and σ_Y^2 are shown in Figures 5.11 and 5.12, respectively. Similar to previous cases, the CC presents a monotonic convergence, while this is not the case for the adaptive methods. Only for $N = 129$, the CC method yields much better results than the new method.

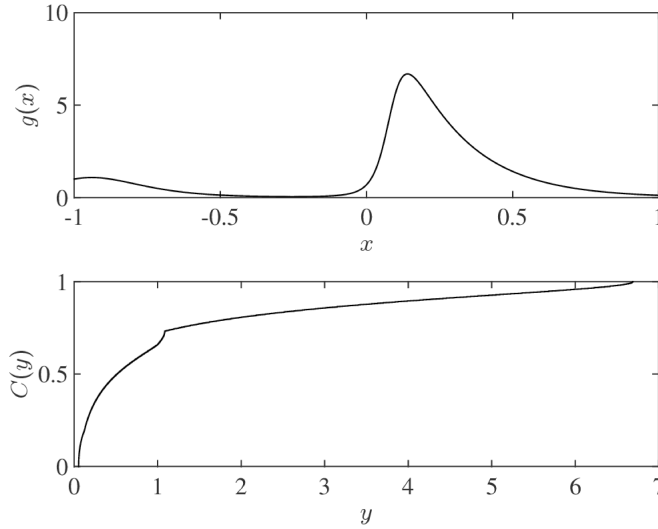


Figure 5.9: Case 3: Lotka-Volterra model. Top panel: $g(x)$; bottom panel: $C(y)$.

5.3.4 Case 4: Van der Pol oscillator

Our last example is the celebrated Van der Pol oscillator[112, 75, 113, 114], which has been extensively studied as a textbook case of a nonlinear dynamical system. In this respect this test case is very relevant to Uncertainty Quantification, since real systems often exhibit a high degree of nonlinearity. Similar to Case 3, we define our test function $g(x)$ as the output of a set of two ODEs, which we solve numerically with MATLAB. The model for the Van der Pol oscillator is:

$$\frac{dQ(t)}{dt} = V(t) \tag{5.17}$$

$$\frac{dV(t)}{dt} = (-50 + 100(x + 2))(1 - Q(t)^2)V(t) - Q(t). \tag{5.18}$$

The initial conditions are $Q(t = 0) = 2$, $V(t = 0) = 0$. The model is solved for time $t \in [0, 300]$, and the function $g(x)$ is defined as

$$g(x) = V(t = 300, x). \tag{5.19}$$

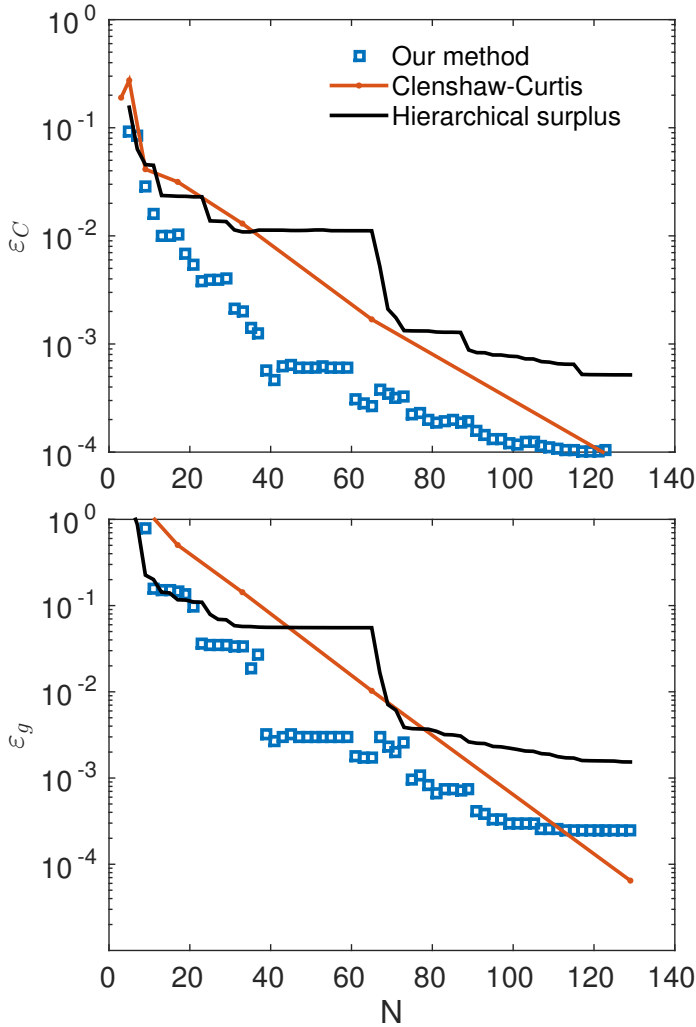


Figure 5.10: Case 3. Error ε_C (top) ε_g (bottom) as function of number of sampling points N . Blue squares: new adaptive selection method. Red dots: Clenshaw-Curtis. Black curve: adaptive method based on hierarchical surplus.

The so-called nonlinear damping parameter is rescaled such that for $x \in [-1, 1]$, it ranges between 50 and 250. The function $g(x)$ and the corresponding cdf $C(y)$ are shown in Figure 5.13. This function is clearly much more challenging than the previous ones. It is divided in two branches, where it takes values $-2 \leq y \leq -1$ and $1 \leq y \leq 2$, and it presents discontinuities where it jumps from one branch to the other. Correspondingly, cdf $C(y)$ presents a flat plateau for $-1 \leq y \leq 1$, which is the major challenge for both methods. In figure 5.14

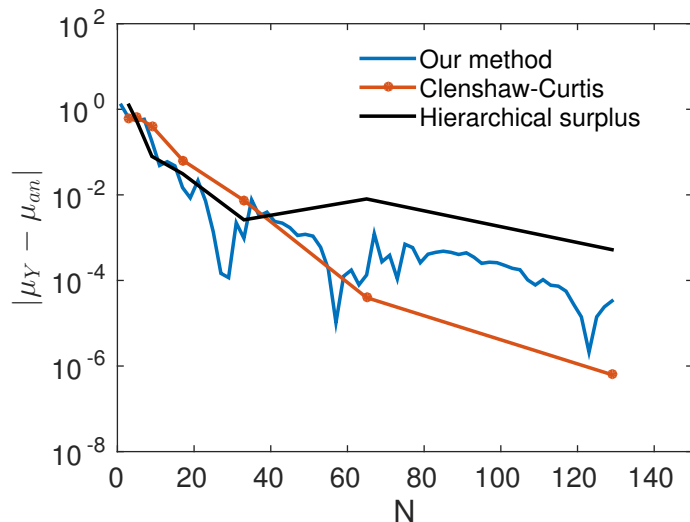


Figure 5.11: Case 3. Absolute error in the mean μ_Y versus number of sampling points N . Blue: new adaptive selection method. Red: Clenshaw-Curtis. Black: adaptive method based on hierarchical surplus.

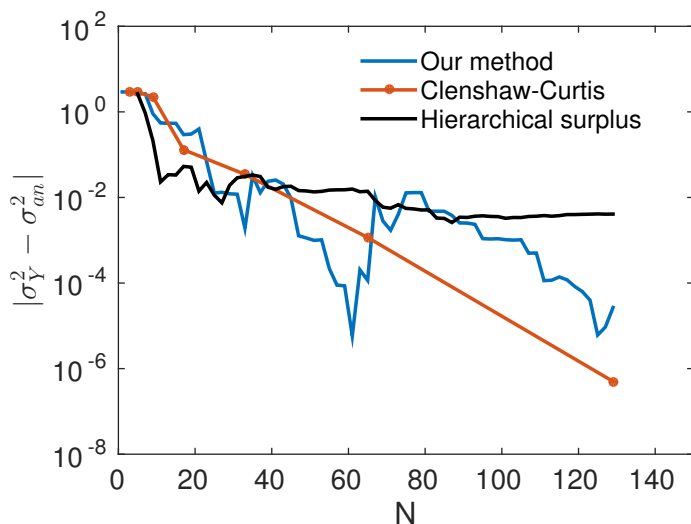


Figure 5.12: Case 3. Absolute error in the variance σ_Y^2 versus number of sampling points N . Blue: new adaptive selection method. Red: Clenshaw-Curtis. Black: adaptive method based on hierarchical surplus.

we show the errors ε_g and ε_C . The overall convergence rate of the CC and the new method is similar. For this case, the hierarchical surplus method yields a

better convergence, but only for $N > 80$. As we commented before, the mean μ_Y has no statistical meaning in this case, because the output is divided into two separate regions. The convergence for σ_Y^2 is presented in Figure 5.15.

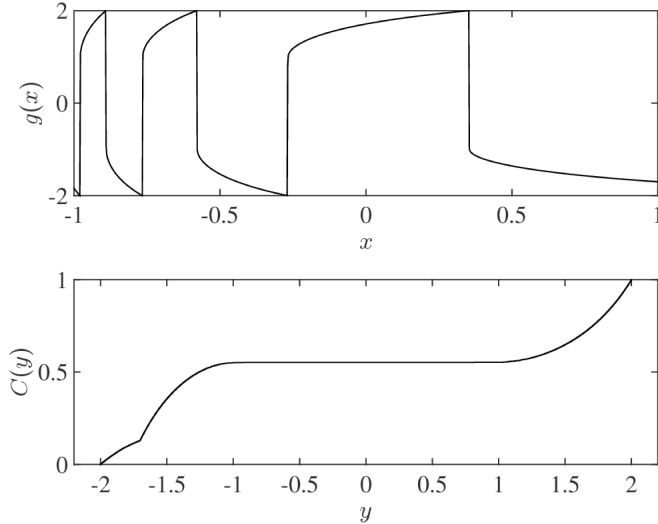


Figure 5.13: Case 4: Van der Pol oscillator. Top panel: $g(x)$; bottom panel: $C(y)$.

5.4 Conclusions and future work

We have presented a new adaptive algorithm for the selection of sampling points for non-intrusive stochastic collocation in Uncertainty Quantification (UQ). The main idea is to use a radial basis function as interpolant, and to refine the grid on points where the interpolant presents large and small first derivative.

In this work we have focused on 1D and uniform probability $P_X(x)$, and we have shown four test cases, encompassing analytical and non-analytical smooth functions, which are prototype of a very wide class of functions. In all cases the new adaptive method improved the efficiency of both the (non-adaptive) Clenshaw-Curtis collocation method, and of the adaptive algorithm based on the calculation of the hierarchical surplus (note that the method used in this paper is a slight improvement of the classical algorithm). The strength of our method is the ability to select a new sampling point making full use of the interpolant resulting from all the previous evaluation of the function $g(x)$, thus seeking the most optimal convergence rate for the cdf $C(y)$. We have shown that there is no one-to-one correspondence between a reduction in the interpolation error ε_g and a reduction in the cdf error ε_C . For this reason, collocation methods that choose

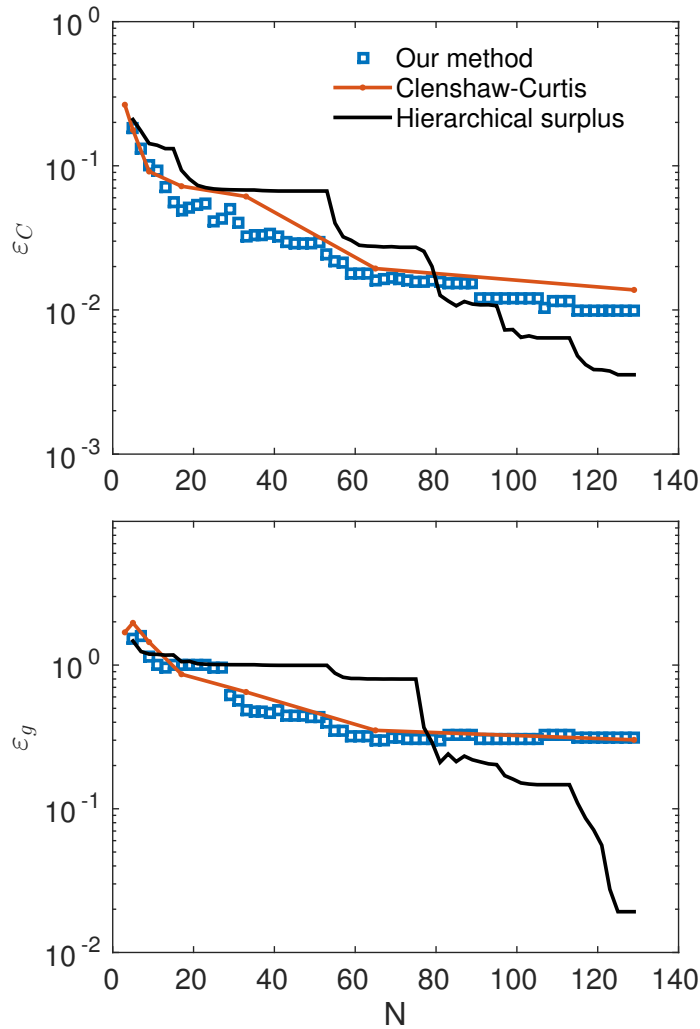


Figure 5.14: Case 4. Error ϵ_C (top) ϵ_g (bottom) as function of number of sampling points N . Blue squares: new adaptive selection method. Red dots: Clenshaw-Curtis. Black curve: adaptive method based on hierarchical surplus.

the distribution of sampling points a priori can perform poorly in attaining a fast convergence rate in ϵ_C , which is the main goal of UQ. Moreover, in order to maintain the nestedness of the collocation points the CC method requires larger and larger number of simulations (2^w moving from level w to level $w + 1$), which is in contrast with our new method where one can add one point at the time. We envision many possible research directions to further investigate our method. The most obvious is to study multi-dimensional problems. We emphasize that

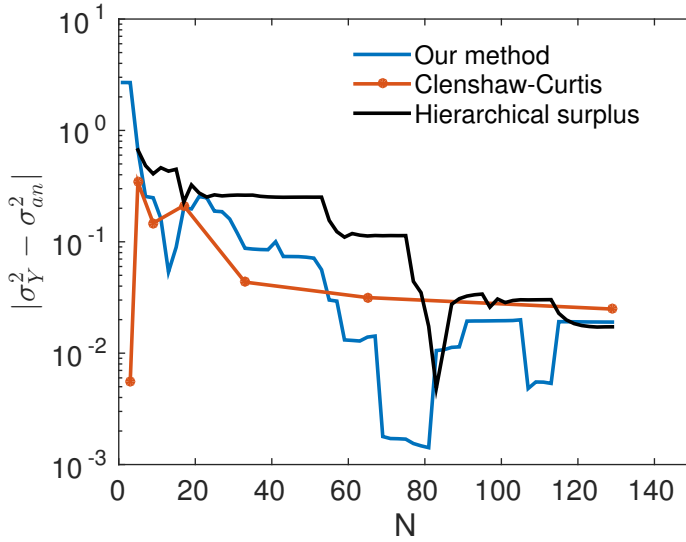


Figure 5.15: Case 4. Absolute error in the variance σ_Y^2 versus number of sampling points N . Blue: new adaptive selection method. Red: Clenshaw-Curtis. Black: adaptive method based on hierarchical surplus.

the radial basis function is a mesh-free method and as such we anticipate that this will largely alleviate the curse of dimensionality that afflicts other collocation methods based on quadrature points (however, see [94] for methods related to the construction of sparse grids, which have the same aim). Moreover, it will be interesting to explore the versatility of RBF in what concerns the possibility of choosing an optimal shape parameter c [115]. Recent work [116, 117] investigated the role of the shape parameter c in interpolating discontinuous functions, which might be very relevant in the context of UQ, when the continuity of $g(x)$ cannot be assumed a priori. Finally, a very appealing research direction, would be to simultaneously exploit quasi-Monte Carlo and adaptive selection methods for extremely large dimension problems.

Chapter 6

Conclusions & Outlook

Here we summarize the conclusions of this thesis. We also present an outlook about how the work could be utilized to build models for electric discharge simulations comprising more scales in a computationally efficient manner.

6.1 Conclusions

Broadly speaking, the work presented in this thesis can be summarized under 3 categories. They are

- Physical/mathematical model development (Chapter 2, 3, 4)
- Code development and testing (Chapter 2, 5)
- Usage of the code for simulations (Chapter 3, 4, 5)

Here are the conclusions of the different chapters:

- **Chapter 2**

Some numerical test results are presented for the numerical discretization techniques used in later chapters. The test results accurately captured the essential features of the reference solutions thereby establishing the correctness of the results generated from software developed.

- **Chapter 3**

The evolution of a coupled system of electric discharge and background gas in a short plane-to-plane electrode configuration in 2D-cylindrical symmetry was simulated. It was shown that with a simple model consisting of electron impact ionization and secondary electrode emission, simple relationships between the transport coefficients and gas density and heat transfer from the electric discharge to the gas, one can understand the formation of a spark. Particularly one can see how heat induced changes in the background gas density can trigger ionization in the discharge channel leading to breakdown even though initially the electric field is everywhere below the breakdown value. The dynamics was evaluated in high pressure nitrogen.

- **Chapter 4**

In the previous chapter, the discharge dynamics was evaluated only on the ion time scale while the electron dynamics was adiabatically eliminated. In the present chapter the process is reconsidered, now starting from the full electron time scale. The reduced model on the ion time scale (as used in Chapter 3) is derived, and it is tested in a 1D model when the reduced model can be used to speed up the simulations. Then results on the thermally driven break-down process of air at standard temperature and pressure in a short gap in 2D cylindrical symmetry are presented where the simulation was switched manually between full and reduced discharge model, as appropriate.

- **Chapter 5**

A new strategy for the selection of sampling points in Uncertainty Quan-

tification was presented. The goal was to achieve the fastest possible convergence in the cumulative distribution function of a stochastic output of interest. This strategy enabled adaptively adding new sampling points one at a time. It took the previous evaluations of the target nonlinear function into account. Comparisons with a stochastic collocation method based on the Clenshaw-Curtis quadrature rule, and with an adaptive method based on hierarchical surplus were presented showing that the new method often results in a large computational saving.

6.2 Outlook

The role of gas heating in electric discharges continues to be investigated with better models due to the availability of increased computational power, good quality cross-sectional data and industrial interest where modern applications demand better understanding of the underlying physics. In the current work we have tackled some of the challenges which one faces while modeling the role of heating. In particular, the coupling of the electric discharge model with the gas dynamics model in 3D assuming cylindrical symmetry and switching between the full and the reduced model of electrical discharge for computational efficiency are two key elements of this work. We applied the developed models to simulate heat driven electrical breakdown in two different gas media. A significant challenge will be to extend the models to full 3D and to incorporate plasma chemistry models. We also proposed an adaptive sampling strategy for uncertainty quantification. Since a lot of the simulation work depends on the quality of the cross-sectional data and the transport data, it will be beneficial to do uncertainty quantification studies on the results obtained to establish their robustness. Here, the proposed strategy might be employed. All the tools and models developed here can be used to build better quantitative understanding of electrical discharge processes. On a holistic level, the models developed may possibly be integrated in the suite of tools available for electric discharge simulation.

Bibliography

- [1] Anna Dubinova et al. “Prediction of lightning inception by large ice particles and extensive air showers”. In: *Physical review letters* 115.1 (2015), p. 015002.
- [2] C Rutjes et al. “TGF afterglows: A new radiation mechanism from thunderstorms”. In: *Geophysical Research Letters* 44.20 (2017).
- [3] LR Grabowski et al. “Corona above water reactor for systematic study of aqueous phenol degradation”. In: *Plasma Chemistry and Plasma Processing* 26.1 (2006), pp. 3–17.
- [4] JS Clements et al. “Combined Removal of SO₂ NO_x and Fly Ash from Flue Gas Using Pulsed Streamer Corona”. In: *Proceedings of 1986 IEEE-IAS Annual Meeting*. 1986, pp. 1183–1190.
- [5] GJJ Winands et al. “An industrial streamer corona plasma system for gas cleaning”. In: *IEEE transactions on plasma science* 34.5 (2006), pp. 2426–2433.
- [6] Gregory Fridman et al. “Applied plasma medicine”. In: *Plasma Processes and Polymers* 5.6 (2008), pp. 503–533.
- [7] Natalia Yu Babaeva and Mark J Kushner. “Dynamics of dielectric barrier discharges over wounded skin”. In: *IEEE Transactions on Plasma Science* 39.11 (2011), pp. 2964–2965.
- [8] Eric Moreau. “Airflow control by non-thermal plasma actuators”. In: *Journal of physics D: applied physics* 40.3 (2007), p. 605.
- [9] Andrey Starikovskiy and Nickolay Aleksandrov. “Plasma-assisted ignition and combustion”. In: *Progress in Energy and Combustion Science* 39.1 (2013), pp. 61–110.
- [10] Hiromitsu Matsuno et al. *Dielectric barrier discharge lamp*. US Patent 5,666,026. Sept. 1997.
- [11] Ulrich Kogelschatz, Baldur Eliasson, and Walter Egli. “From ozone generators to flat television screens: history and future potential of dielectric-barrier discharges”. In: *Pure and Applied Chemistry* 71.10 (1999), pp. 1819–1828.

- [12] Mounir Laroussi. “Sterilization of contaminated matter with an atmospheric pressure plasma”. In: *IEEE Transactions on Plasma Science* 24.3 (1996), pp. 1188–1191.
- [13] Richard Blackburn. *Sustainable textiles: life cycle and environmental impact*. Elsevier, 2009.
- [14] J Zhang et al. “Numerical and experimental investigation of dielectric recovery in supercritical N₂”. In: *Plasma Sources Science and Technology* 24.2 (2015), p. 025008.
- [15] Toshiyuki Uchii et al. “Fundamental research on SF₆-free gas insulated switchgear adopting CO₂ gas and its mixtures”. In: *Proceedings of International Symposium on EcoTopia Science*. 2007, pp. 516–520.
- [16] Patrick C Stoller et al. “CO₂ as an Arc Interruption Medium in Gas Circuit Breakers”. In: *IEEE Transactions on Plasma Science* 41.8 (2013), pp. 2359–2369.
- [17] Ken Beauchamp. *History of telegraphy*. 26. Iet, 2001.
- [18] S Dujko et al. “High-order fluid model for streamer discharges: I. Derivation of model and transport data”. In: *Journal of Physics D: Applied Physics* 46.47 (2013), p. 475202.
- [19] AH Markosyan, S Dujko, and U Ebert. “High-order fluid model for streamer discharges: II. Numerical solution and investigation of planar fronts”. In: *Journal of Physics D: Applied Physics* 46.47 (2013), p. 475203.
- [20] Anna Alexandrovna Dubinova. *Modeling of streamer discharges near dielectrics*. TU Eindhoven, 2016.
- [21] J. Teunissen. *3D simulations and analysis of pulsed discharges*. TU Eindhoven, 2015.
- [22] Carolynne Montijn, Willem Hundsdorfer, and Ute Ebert. “An adaptive grid refinement strategy for the simulation of negative streamers”. In: *Journal of Computational Physics* 219.2 (2006), pp. 801–835.
- [23] Barry Koren. “A robust upwind discretization method for advection, diffusion and source terms”. In: *Department of Numerical Mathematics [NM]* R 9308 (1993).
- [24] Carolynne Montijn and Ute Ebert. “Diffusion correction to the Raether–Meek criterion for the avalanche-to-streamer transition”. In: *Journal of Physics D: Applied Physics* 39.14 (2006), p. 2979.
- [25] Gary A Sod. “A survey of several finite difference methods for systems of nonlinear hyperbolic conservation laws”. In: *Journal of computational physics* 27.1 (1978), pp. 1–31.

-
- [26] Alexander Kurganov and Eitan Tadmor. “Solution of two-dimensional Riemann problems for gas dynamics without Riemann problem solvers”. In: *Numerical Methods for Partial Differential Equations* 18.5 (2002), pp. 584–608.
- [27] K Mochizuki et al. “Evaluation of interruption capability on various gases”. In: *Gaseous Dielectrics X*. Springer, 2004, pp. 265–270.
- [28] Nazar Hussain Malik, AA Al-Arainy, and Mohammad Iqbal Qureshi. *Electrical insulation in power systems*. Marcel Dekker, 1998.
- [29] Steven A Boggs. “Sulphur Hexafluoride-A complex dielectric”. In: *IEEE Electrical Insulation Magazine* 5.6 (1989), pp. 16–21.
- [30] A Lee and LS Frost. “Interruption capability of gases and gas mixtures in a puffer-type interrupter”. In: *IEEE Transactions on Plasma Science* 8.4 (1980), pp. 362–367.
- [31] Masayuki Hikita et al. “Insulation characteristics of gas mixtures including perfluorocarbon gas”. In: *IEEE Transactions on Dielectrics and Electrical Insulation* 15.4 (2008).
- [32] J Zhang et al. “Breakdown strength and dielectric recovery in a high pressure supercritical nitrogen switch”. In: *IEEE Transactions on Dielectrics and Electrical Insulation* 22.4 (2015), pp. 1823–1832.
- [33] NA Popov. “Formation and development of a leader channel in air”. In: *Plasma Physics Reports* 29.8 (2003), pp. 695–708.
- [34] Ute Ebert et al. “Review of recent results on streamer discharges and discussion of their relevance for sprites and lightning”. In: *Journal of Geophysical Research: Space Physics* 115.A7 (2010).
- [35] Anbang Sun, Jannis Teunissen, and Ute Ebert. “The inception of pulsed discharges in air: simulations in background fields above and below breakdown”. In: *Journal of Physics D: Applied Physics* 47.44 (2014), p. 445205.
- [36] Fabien Tholin and Anne Bourdon. “Simulation of the hydrodynamic expansion following a nanosecond pulsed spark discharge in air at atmospheric pressure”. In: *Journal of Physics D: Applied Physics* 46.36 (2013), p. 365205.
- [37] Atsushi Komuro and Ryo Ono. “Two-dimensional simulation of fast gas heating in an atmospheric pressure streamer discharge and humidity effects”. In: *Journal of Physics D: Applied Physics* 47.15 (2014), p. 155202.
- [38] AA Kulikovskiy. “Positive streamer between parallel plate electrodes in atmospheric pressure air”. In: *Journal of physics D: Applied physics* 30.3 (1997), p. 441.

- [39] Ismail R Rafatov, Danijela D Šijačić, and Ute Ebert. “Spatiotemporal patterns in a dc semiconductor-gas-discharge system: Stability analysis and full numerical solutions”. In: *Physical Review E* 76.3 (2007), p. 036206.
- [40] Danijela D Šijačić, Ute Ebert, and Ismail Rafatov. “Oscillations in dc driven barrier discharges: Numerical solutions, stability analysis, and phase diagram”. In: *Physical Review E* 71.6 (2005), p. 066402.
- [41] Eleuterio F Toro. *Riemann solvers and numerical methods for fluid dynamics: a practical introduction*. Springer Science & Business Media, 2013.
- [42] Fabien Tholin and Anne Bourdon. “Simulation of the stable ‘quasi-periodic’ glow regime of a nanosecond repetitively pulsed discharge in air at atmospheric pressure”. In: *Plasma Sources Science and Technology* 22.4 (2013), p. 045014.
- [43] O Eichwald et al. “Modeling and three-dimensional simulation of the neutral dynamics in an air discharge confined in a microcavity. I. Formation and free expansion of the pressure waves”. In: *Journal of applied physics* 84.9 (1998), pp. 4704–4715.
- [44] O Eichwald et al. “Modeling and three dimensional simulation of the neutral dynamics in an air discharge confined in a microcavity. II. Analysis of the wall and geometry effects”. In: *Journal of applied physics* 84.9 (1998), pp. 4716–4726.
- [45] Jeremy A Rioussset, Victor P Pasko, and Anne Bourdon. “Air-density-dependent model for analysis of air heating associated with streamers, leaders, and transient luminous events”. In: *Journal of Geophysical Research: Space Physics* 115.A12 (2010).
- [46] Randall J LeVeque. *Finite volume methods for hyperbolic problems*. Vol. 31. Cambridge university press, 2002.
- [47] *Clawpack webpage*. <http://www.clawpack.org/>.
- [48] Haim Nessyahu and Eitan Tadmor. “Non-oscillatory central differencing for hyperbolic conservation laws”. In: *Journal of computational physics* 87.2 (1990), pp. 408–463.
- [49] Willem Hundsdorfer and Jan G Verwer. *Numerical solution of time-dependent advection-diffusion-reaction equations*. Vol. 33. Springer Science & Business Media, 2013.
- [50] *FISHPACK webpage*. <http://www.netlib.org/cgi-bin/search.pl>.
- [51] Sergey Pancheshnyi. “Role of electronegative gas admixtures in streamer start, propagation and branching phenomena”. In: *Plasma Sources Science and Technology* 14.4 (2005), p. 645.

-
- [52] JJ Lowke. “Theory of electrical breakdown in air—the role of metastable oxygen molecules”. In: *Journal of Physics D: Applied Physics* 25.2 (1992), p. 202.
- [53] NA Popov. “Investigation of the mechanism for rapid heating of nitrogen and air in gas discharges”. In: *Plasma physics reports* 27.10 (2001), pp. 886–896.
- [54] NL Aleksandrov et al. “Mechanism of ultra-fast heating in a non-equilibrium weakly ionized air discharge plasma in high electric fields”. In: *Journal of Physics D: Applied Physics* 43.25 (2010), p. 255201.
- [55] NA Popov. “Fast gas heating in a nitrogen–oxygen discharge plasma: I. Kinetic mechanism”. In: *Journal of Physics D: Applied Physics* 44.28 (2011), p. 285201.
- [56] Diane Rusterholtz et al. “Ultrafast heating in nanosecond discharges in atmospheric pressure air”. In: *50th AIAA Aerospace Sciences Meeting including the New Horizons Forum and Aerospace Exposition*. 2012, p. 509.
- [57] V Guerra, PA Sá, and J Loureiro. “Kinetic modeling of low-pressure nitrogen discharges and post-discharges”. In: *The European Physical Journal-Applied Physics* 28.2 (2004), pp. 125–152.
- [58] SM Starikovskaia. “Plasma assisted ignition and combustion”. In: *Journal of Physics D: Applied Physics* 39.16 (2006), R265.
- [59] E Marode, F Bastien, and M Bakker. “A model of the streamer-induced spark formation based on neutral dynamics”. In: *Journal of Applied Physics* 50.1 (1979), pp. 140–146.
- [60] F Bastien and E Marode. “Breakdown simulation of electronegative gases in non-uniform field”. In: *Journal of Physics D: Applied Physics* 18.3 (1985), p. 377.
- [61] MN Shneider. “Turbulent decay of after-spark channels”. In: *Physics of Plasmas* 13.7 (2006), p. 073501.
- [62] Samira Kacem et al. “Simulation of expansion of thermal shock and pressure waves induced by a streamer dynamics in positive dc corona discharges”. In: *IEEE Transactions on Plasma Science* 41.4 (2013), pp. 942–947.
- [63] Ashutosh Agnihotri, Willem Hundsdorfer, and Ute Ebert. “Coupling discharge and gas dynamics in streamer-less spark formation in supercritical N₂”. In: *Japanese Journal of Applied Physics* 55.7S2 (2016), p. 07LD06.
- [64] AV Phelps and LC Pitchford. “Anisotropic scattering of electrons by N₂ and its effect on electron transport”. In: *Physical Review A* 31.5 (1985), p. 2932.

- [65] SA Lawton and AV Phelps. “Excitation of the $b\ 1\Sigma^+ g$ state of O_2 by low energy electrons”. In: *The Journal of Chemical Physics* 69.3 (1978), pp. 1055–1068.
- [66] Ryo Ono, Yoshiyuki Teramoto, and Tetsuji Oda. “Gas density in a pulsed positive streamer measured using laser shadowgraph”. In: *Journal of Physics D: Applied Physics* 43.34 (2010), p. 345203.
- [67] Atsushi Komuro, Kazunori Takahashi, and Akira Ando. “Numerical simulation for the production of chemically active species in primary and secondary streamers in atmospheric-pressure dry air”. In: *Journal of Physics D: Applied Physics* 48.21 (2015), p. 215203.
- [68] Alexander Kurganov and Eitan Tadmor. “New high-resolution central schemes for nonlinear conservation laws and convection–diffusion equations”. In: *Journal of Computational Physics* 160.1 (2000), pp. 241–282.
- [69] Dongbin Xiu. “Fast numerical methods for stochastic computations: a review”. In: *Communications in computational physics* 5.2-4 (2009), pp. 242–272.
- [70] MS Eldred and John Burkardt. “Comparison of non-intrusive polynomial chaos and stochastic collocation methods for uncertainty quantification”. In: *AIAA paper 976.2009* (2009), pp. 1–20.
- [71] G Onorato et al. “Comparison of intrusive and non-intrusive polynomial chaos methods for CFD applications in aeronautics”. In: *V European Conference on Computational Fluid Dynamics ECCOMAS, Lisbon, Portugal*. 2010, pp. 14–17.
- [72] Dongbin Xiu and George Em Karniadakis. “The Wiener–Askey polynomial chaos for stochastic differential equations”. In: *SIAM journal on scientific computing* 24.2 (2002), pp. 619–644.
- [73] Thierry Crestaux, Olivier Le Maître, and Jean-Marc Martinez. “Polynomial chaos expansion for sensitivity analysis”. In: *Reliability Engineering & System Safety* 94.7 (2009), pp. 1161–1172.
- [74] Kanali Togawa, Andrea Benigni, and Antonello Monti. “Advantages and challenges of non-intrusive polynomial chaos theory”. In: *Proceedings of the 2011 Grand Challenges on Modeling and Simulation Conference*. Society for Modeling & Simulation International. 2011, pp. 30–35.
- [75] Michael Scott Eldred. “Recent advances in non-intrusive polynomial chaos and stochastic collocation methods for uncertainty analysis and design”. In: *AIAA Paper 2274.2009* (2009), p. 37.
- [76] Ivo Babuska, Raúl Tempone, and Georgios E Zouraris. “Galerkin finite element approximations of stochastic elliptic partial differential equations”. In: *SIAM Journal on Numerical Analysis* 42.2 (2004), pp. 800–825.

-
- [77] Mircea Grigoriu. *Stochastic systems: uncertainty quantification and propagation*. Springer Science & Business Media, 2012.
- [78] Dongbin Xiu. *Numerical methods for stochastic computations: a spectral method approach*. Princeton university press, 2010.
- [79] Olivier Le Maitre and Omar M Knio. *Spectral methods for uncertainty quantification: with applications to computational fluid dynamics*. Springer Science & Business Media, 2010.
- [80] Russel E Caffisch. “Monte carlo and quasi-monte carlo methods”. In: *Acta numerica* 7 (1998), pp. 1–49.
- [81] Malvin H Kalos and Paula A Whitlock. *Monte carlo methods*. John Wiley & Sons, 2008.
- [82] Pierre L’Ecuyer and Art B Owen. *Monte Carlo and Quasi-Monte Carlo Methods 2008*. Springer, 2009.
- [83] Harald Niederreiter. “Quasi-Monte Carlo methods and pseudo-random numbers”. In: *Bulletin of the American Mathematical Society* 84.6 (1978), pp. 957–1041.
- [84] Malvin H Kalos and Paula A Whitlock. “Pseudorandom numbers”. In: *Monte Carlo Methods, Second Edition* (2008), pp. 179–197.
- [85] Richard Bellman. *Dynamic programming*. Courier Corporation, 2013.
- [86] Piotr Indyk and Rajeev Motwani. “Approximate nearest neighbors: towards removing the curse of dimensionality”. In: *Proceedings of the thirtieth annual ACM symposium on Theory of computing*. ACM. 1998, pp. 604–613.
- [87] Frances Y Kuo and Ian H Sloan. “Lifting the curse of dimensionality”. In: *Notices of the AMS* 52.11 (2005), pp. 1320–1328.
- [88] Dongbin Xiu and Jan S Hesthaven. “High-order collocation methods for differential equations with random inputs”. In: *SIAM Journal on Scientific Computing* 27.3 (2005), pp. 1118–1139.
- [89] Jasmine Foo and George Em Karniadakis. “Multi-element probabilistic collocation method in high dimensions”. In: *Journal of Computational Physics* 229.5 (2010), pp. 1536–1557.
- [90] Ivo Babuška, Fabio Nobile, and Raul Tempone. “A stochastic collocation method for elliptic partial differential equations with random input data”. In: *SIAM Journal on Numerical Analysis* 45.3 (2007), pp. 1005–1034.
- [91] Peng Wang and Daniel M Tartakovsky. “Uncertainty quantification in kinematic-wave models”. In: *Journal of computational Physics* 231.23 (2012), pp. 7868–7880.

- [92] Peng Wang et al. “CDF Solutions of Buckley–Leverett Equation with Uncertain Parameters”. In: *Multiscale Modeling & Simulation* 11.1 (2013), pp. 118–133.
- [93] Sergey Smolyak. “Quadrature and interpolation formulas for tensor products of certain classes of functions”. In: *Soviet Math. Dokl.* Vol. 4. 1963, pp. 240–243.
- [94] Baskar Ganapathysubramanian and Nicholas Zabaras. “Sparse grid collocation schemes for stochastic natural convection problems”. In: *Journal of Computational Physics* 225.1 (2007), pp. 652–685.
- [95] Marcel Bieri, Roman Andreev, and Christoph Schwab. “Sparse tensor discretization of elliptic SPDEs”. In: *SIAM Journal on Scientific Computing* 31.6 (2009), pp. 4281–4304.
- [96] Xiang Ma and Nicholas Zabaras. “An adaptive hierarchical sparse grid collocation algorithm for the solution of stochastic differential equations”. In: *Journal of Computational Physics* 228.8 (2009), pp. 3084–3113.
- [97] Fabio Nobile, Raúl Tempone, and Clayton G Webster. “A sparse grid stochastic collocation method for partial differential equations with random input data”. In: *SIAM Journal on Numerical Analysis* 46.5 (2008), pp. 2309–2345.
- [98] John D Jakeman and Stephen G Roberts. “Local and dimension adaptive stochastic collocation for uncertainty quantification”. In: *Sparse grids and applications*. Springer, 2012, pp. 181–203.
- [99] Ngoc-Hien Nguyen, Karen Willcox, and Boo Cheong Khoo. “Model order reduction for stochastic optimal control”. In: *ASME 2012 11th Biennial Conference on Engineering Systems Design and Analysis*. American Society of Mechanical Engineers. 2012, pp. 2–4.
- [100] Dirk P Laurie. “Computation of Gauss-type quadrature formulas”. In: *Journal of Computational and Applied Mathematics* 127.1 (2001), pp. 201–217.
- [101] Walter Gautschi. “On the construction of Gaussian quadrature rules from modified moments.” In: *Mathematics of Computation* 24.110 (1970), pp. 245–260.
- [102] Jörg Waldvogel. “Fast construction of the Fejér and Clenshaw–Curtis quadrature rules”. In: *BIT Numerical Mathematics* 46.1 (2006), pp. 195–202.
- [103] Jean-Paul Berrut and Lloyd N Trefethen. “Barycentric lagrange interpolation”. In: *Siam Review* 46.3 (2004), pp. 501–517.
- [104] Lloyd N Trefethen. *Spectral methods in MATLAB*. SIAM, 2000.

-
- [105] James F Epperson. “On the Runge example”. In: *Amer. Math. Monthly* 94.4 (1987), pp. 329–341.
- [106] Xiang Ma and Nicholas Zabaras. “An efficient Bayesian inference approach to inverse problems based on an adaptive sparse grid collocation method”. In: *Inverse Problems* 25.3 (2009), p. 035013.
- [107] Jeroen AS Witteveen and Gianluca Iaccarino. “Refinement criteria for simplex stochastic collocation with local extremum diminishing robustness”. In: *SIAM Journal on Scientific Computing* 34.3 (2012), A1522–A1543.
- [108] John P Boyd. *Chebyshev and Fourier spectral methods*. Courier Corporation, 2001.
- [109] Fred Brauer, Carlos Castillo-Chavez, and Carlos Castillo-Chavez. *Mathematical models in population biology and epidemiology*. Vol. 40. Springer, 2001.
- [110] M Henry H Stevens. “Lotka–volterra interspecific competition”. In: *A Primer of Ecology with R*. Springer, 2009, pp. 135–159.
- [111] Peter J Wangersky. “Lotka-Volterra population models”. In: *Annual Review of Ecology and Systematics* 9.1 (1978), pp. 189–218.
- [112] Mohammad B Dadfar, James Geer, and Carl M Andersen. “Perturbation analysis of the limit cycle of the free van der Pol equation”. In: *SIAM Journal on Applied Mathematics* 44.5 (1984), pp. 881–895.
- [113] Ruoshi Yuan et al. “Exploring a noisy van der Pol type oscillator with a stochastic approach”. In: *Physical Review E* 87.6 (2013), p. 062109.
- [114] Liping Liu, Earl H Dowell, and Kenneth C Hall. “A novel harmonic balance analysis for the Van Der Pol oscillator”. In: *International Journal of Non-Linear Mechanics* 42.1 (2007), pp. 2–12.
- [115] Gregory E Fasshauer and Jack G Zhang. “On choosing “optimal” shape parameters for RBF approximation”. In: *Numerical Algorithms* 45.1 (2007), pp. 345–368.
- [116] Jae-Hun Jung and Vincent R Durante. “An iterative adaptive multi-quadratic radial basis function method for the detection of local jump discontinuities”. In: *Applied Numerical Mathematics* 59.7 (2009), pp. 1449–1466.
- [117] JG Wang and GR Liu. “On the optimal shape parameters of radial basis functions used for 2-D meshless methods”. In: *Computer methods in applied mechanics and engineering* 191.23 (2002), pp. 2611–2630.

Acknowledgements

These past four years have been a journey full of memorable events and wonderful companionships which I will cherish throughout my lifetime. First and foremost, I have been incredibly lucky with the opportunities that came by my way and the people that I met so far. My deepest gratitude goes to my supervisors, Ute and Willem, who not only gave me the opportunity to come to The Netherlands and pursue research at CWI but simultaneously challenged and encouraged me to think and follow my own ideas. There were times when I felt directionless and things seemed to get stuck, but Ute always made sure that I rowed the boat in the right direction and Willem ensured that the boat had no holes! I thank you both for the relentless patience and support that you provided me. It's a very sad feeling to write this acknowledgement with Willem not around. I will always remember his wise judgement and welcoming nature.

Casper, my colleague and my dear friend, thank you for being my office neighbor. I will always remember the times we spent together at CWI and beyond, and the chats we had. You were there to pull me up whenever I got "locked in a local minimum". The conversations that I had with you about the future and life always left me wondering about the breadth of your thought. I thank you and Laura for choosing me to sign your wedding papers. Believe me, I was extremely nervous. I hope I signed my own name :).

Enrico, aside from being a colleague you have been a mentor and a friend. Your directness and your approach to cut through the complexity of any process and grasp what is essential has continued to amaze me. I could talk to you practically about any problem I had, technical or otherwise. Your door was always open to discuss and argue about the next big question. The after-lunch visits to coffee machine in the library was always something I looked forward to and will miss forever. And do not forget the occasional excursions to the NIKHEF coke/coffee machine. The sound of the coins is still very fresh in my head!

Mandar and Gabriel, you guys have been the perfect office mates. Mandar, I always enjoyed our ping pong sessions and felt quite satisfied whenever I could get past your block which was rare. The thoughtful rants about the state of the current technology landscape and the latest trends in software programming/engineering were good food for the brain. And Gabriel, it's hard for me to

gauge how many poetic thoughts you have in your head! For everything around, you had an amazing perspective to add. I will always remember the rare long walks we had outside CWI where we shared stories from our hometowns and the similarities between Brazil and India. And not to forget, the manifestation of your hidden energy and anger on a chessboard was a treat to watch! I am certain, one day we will have enough time to play chess together on a physical chessboard, wherever we wish, whenever we wish.

I thank Nada for the robust support system she has been, not just for me but the entire MD group and beyond. She always took care of so many arrangements which made it easier for us to perform our work. Nada, I wonder how you managed to stay calm with all the constant requests you received from us.

Aram and Bram, my two senior mates, I thank you for getting me off the ground while I was starting my PhD. You guys constantly joked and made me feel at home during my first year, which looking back, couldn't have been joyful without you. Behnaaz, Andy and Daniel, although we have had little time to interact, it was fun. I am sure the group will be full of enthusiasm and energy in your presence. I look forward to seeing more of you guys.

Lastly, no amounts of words are enough to thank my loving family for the effort they put to help me reach at this destination. Apeksha, my dear wife and my best friend, without your care and presence, I could have never have achieved anything significant at all. You were there to witness and pick me up in my toughest moments. I deeply cherish the gift of your friendship and thank you for sharing your life with me. It is a privilege. You truly are the most precious diamond I have in my closet! Papa and Mummy, you always hid the difficulties, howsoever big they may be, behind your smile and made everything look so good. I feel incredibly lucky to be your son. Baba and Aai, thank you for your visits and the conversations whenever I wanted to talk about anything at all and at any time of the day. Baba, I hope someday I will be able to appreciate life as you do and learn to remain as calm as you under toughest of circumstances. Vishnu, my younger brother, your wisdom extends far beyond your age. And so, does your music. I didn't get enough occasions to express my gratitude for the silent guardian of the family you have been while I was away from home. Thank you.

Curriculum Vitae

Ashutosh Agnihotri was born in Kanpur, India on June 14, 1989. From 2007 to 2012 he studied basic sciences at the Indian Institute of Science Education & Research (IISER), Pune. In 2012 he obtained a BS-MS Dual Degree with major in Physics and a Master's thesis entitled "Exploring the gravitational stability/instability for a class of spacetime geometries" under the supervision of Dr. Suneeta Vardarajan. In summer of 2012, as a Project Junior Research Fellow at IISER Pune he worked on the project entitled "Emergent Dynamics on Growing Networks with Comparable Time Scales" developing mathematical models to simulate the underlying physics. Thereafter, as a Project Associate in the Department of Civil Engineering at IIT Kanpur he worked as a programmer developing web-based content.

From August 2013 to January 2018 he performed research as a PhD candidate on modeling heat dominated electrical breakdown processes and uncertainty quantification in the Multiscale Dynamics group of prof.dr. U.M. Ebert at Centrum Wiskunde & Informatica (CWI). CWI is the Dutch national institute for mathematics and computer science. The results of the research work are presented in this dissertation.

Summary

Modeling heat dominated electrical breakdown

Gas heating by an electrical discharge and the subsequent gas expansion is an important mechanism in plasma-assisted combustion, atmospheric lightning leaders, circuit breakers etc. Simulating the interaction between discharge dynamics and gas dynamics is challenging due to the multiscale and nonlinear character of the phenomena. The present thesis deals with the development and application of efficient computational models to simulate heat driven electrical breakdown in various media.

The thesis has been setup as follows. In chapter 2 we present the physical models for the electric discharge and the gas as well as the numerical techniques used to perform the simulations. To study the effect of gas heating on the development of the electric discharge and vice versa, the models describing discharge and gas dynamics are coupled. Performing simulations using the coupled model is computationally expensive due to the multiple timescales involved in the system. To alleviate this, a reduced model for electric discharge dynamics on the timescale of ion motion is derived which is then coupled to the gas dynamics model. In chapter 3, the simulation results of this model for high pressure pure nitrogen are presented and discussed. In chapter 4, a similar methodology is applied to study the role of heating in air at atmospheric pressure. In this chapter, during the initial phase the electron dynamics dominates the dynamics and it is crucial to perform the simulations using the full coupled model on the timescale of electron dynamics. As the system evolves in time, the initial seed electrons leave the system and the discharge dynamics is driven by the relatively slowly moving ions. For computational efficiency, we then switch from the full coupled model to the reduced coupled model. The simulation results show how over long timescales (tens of microseconds) electrical breakdown occurs in the gap due to gas heating. We chose a simple heating model where the gas is heated in two stages. In the first stage, a fraction of the electrical energy heats up the gas instantaneously and the remainder is stored in the vibrationally excited states and relaxes over longer timescales. In chapter 5, a different topic pertaining to the field of uncertainty quantification is studied where a new strategy for the selection of sampling points is presented. The goal was to achieve the fastest

possible convergence in the cumulative distribution function of a stochastic output of interest. The method allows to adaptively add new sampling points one at a time, while taking the previous evaluations of the target nonlinear function into account. The performance of the method is compared with some established approaches, showing that the new method often results in a large computational saving. Chapter 6 presents the major conclusions of the research and ends with an outlook.

Scientific Contributions

Journal Publications

- A. Agnihotri, W. Hundsdorfer and U. Ebert. (2017) *Modeling heat dominated electric breakdown in air, with adaptivity to electron or ion time scales*. Plasma Sources Science and Technology, Vol. 26, No. 9: 095003
- E. Camporeale, A. Agnihotri and C. Rutjes. (2017) *Adaptive selection of sampling points for Uncertainty Quantification*. International Journal for Uncertainty Quantification, Vol. 7, No. 4: pp (285-301)
- A. Agnihotri, W. Hundsdorfer and U. Ebert. (2016) *Coupling discharge and gas dynamics in streamer-less spark formation in supercritical N₂*. Japanese Journal of Applied Physics, Vol. 55, No. 7S2: 07LD06.

Oral Presentations

- *Modelling heat dominated electric breakdown in air with adaptivity to electron or ion timescales*. 29th NNV-Symposium on Plasma Physics and Radiation Technology, Lunteren, The Netherlands, March 2016

Poster Presentations

- *Modelling heat dominated electric breakdown in air with adaptivity to electron or ion timescales*. XXXIII International Conference on Phenomena in Ionized Gases, Estoril, Portugal, July 2017
- *Heating dominated inception of pulsed discharges*. 69th Annual Gaseous Electronics Conference, Bochum, Germany, October 2016
- *Heating dominated inception of pulsed discharges*. Computational Sciences for Future Energy Conference, Utrecht, The Netherlands, October 2016
- *Coupling discharge and gas dynamics in streamer-less spark formation*. 28th NNV-Symposium on Plasma Physics and Radiation Technology, Lunteren, The Netherlands, March 2016

- *Coupling discharge and gas dynamics in streamer-less spark formation.* FOM Veldhoven, Veldhoven, The Netherlands, January 2016
- *Coupling discharge and gas dynamics in streamer-less spark formation in supercritical N₂.* 9th ICRP/68th Gaseous Electronics Conference, Honolulu, Hawaii, USA October 2015
- *Coupling discharge and gas dynamics in streamer to glow to spark transition.* ATW Fundamentals of Aerodynamic Flow and Combustion control by Plasmas, Les Houches, France, April 2015
- *Coupling discharge and gas dynamics in streamer to glow to spark transition.* 27th NNV-Symposium on Plasma Physics and Radiation Technology, Lunteren, The Netherlands, March 2015
- *Modeling DC-circuit breakers for long distance electricity transmission.* FOM Veldhoven, Veldhoven, The Netherlands, January 2015
- *Modeling DC-circuit breakers for long distance electricity transmission.* 67th Gaseous Electronics Conference, Raleigh, North Carolina, USA November 2014